C-CAM: Geometric Aspects and Dynamical Formulation

John L. McGregor

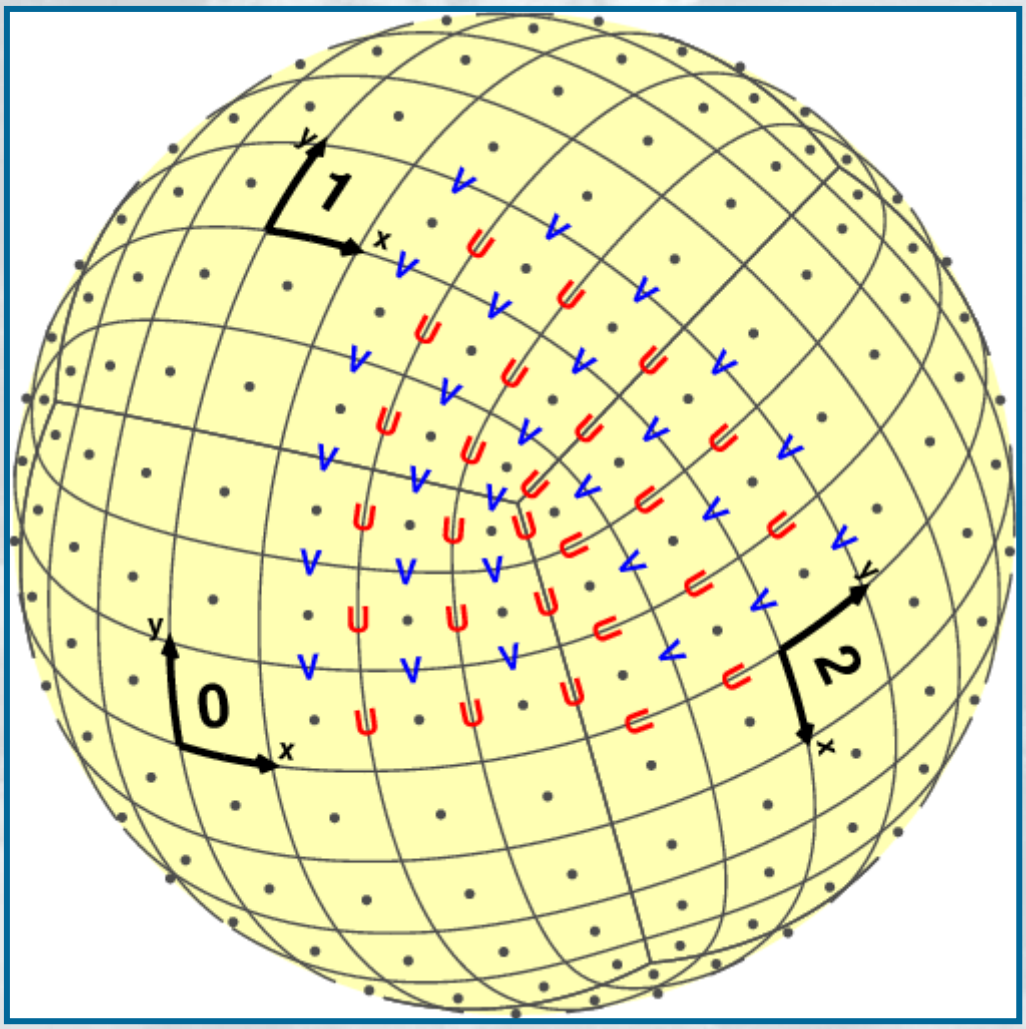

CSIRO
Atmospheric Research
CSIRO Atmospheric Research Technical Paper 70

CSIRO Atmospheric Research No. 70

National Library of Cataloguing-In-Publication entry

McGregor, John L.
C-CAM : geometric aspects and dynamical formulation.

ISBN 0 643 06889 9.

1. Numerical weather forecasting - Mathematical models. 2. Climatology - Mathematical models. I. CSIRO. Division of Atmospheric Research. II. Title. III. Title : Conformal-Cubic Atmospheric Model : geometric aspects and dynamical formulation. (Series : CSIRO Atmospheric Research technical paper (Online) ; no. 70).

551.63

Address and contact details: CSIRO Atmospheric Research
Private Bag No. 1 Aspendale Victoria 3195 Australia
Ph: (+61 3) 9239 4400; fax (+61 3) 9239 4444
Email: ar-enquiries@csiro.au

CSIRO Atmospheric Research Technical Papers may be issued out of sequence. From July 2000 all new Technical Papers will appear on the web site of CSIRO Atmospheric Research. Some Technical Papers will be also appear in paper form.

C-CAM : geometric aspects and dynamical formulation.

John L. McGregor

CSIRO Atmospheric Research Technical Paper No. 70

Contents

1 Introduction

Most global meteorological models are based on a regular latitude-longitude configuration either explicitly, or implicitly, in the case of a spectral formulation. There are, however, advantages in being able to use a grid having more uniform resolution, for reasons of computational economy for a given accuracy and for uniform applicability of physical parameterizations. With this in mind, Sadourny (1972) proposed a grid derived from a gnomonic projection of the cube onto the sphere and presented corresponding solutions of the shallow-water equations. The projection produces six panels covering the sphere; Sadourny (1972) experienced noise problems that he attributed to his low-order finite differencing near the panel edges. McGregor (1997), denoted here by M97, adopted the same grid and demonstrated that the semi-Lagrangian technique of McGregor (1993) permits accurate and noise-free solutions for horizontal advection. With this grid, although the projected grid lines on the cube are orthogonal, the grid lines on the sphere are non-orthogonal. M97 also investigated stretched grids having the same non-orthogonality properties, but producing greater uniformity on the sphere and even better advection results.

Figure 1: An example of a C20 conformal-cubic grid, as viewed from infinity.

The non-orthogonality of the M97 grid creates only slight inconvenience for advection purposes, but the full primitive equations are significantly simpler on an orthogonal grid. Rancic et al. (1996), denoted here by RPM, have fortunately found a solution to this problem. They employ the same Sadourny (1972) projection from the panels of a cube onto the sphere. By means of a conformal mapping with respect to a stereographic projection, they have devised a set of grid lines on each panel of the sphere that are orthogonal to one another except at the vertices where they intersect at 120^o. The grid may be described as a conformal-cubic (C-C) grid and is an example of a modified cubic gnomonic projection The RPM paper is concerned with geometrical properties

of the grid; it also successfully provides Eulerian finite-difference solutions to the shallow-water equations. This report provides details of the global climate model developed at CSIRO known as the Conformal-Cubic Atmospheric Model (C-CAM).

Sadourny (1972), M97 and McGregor (1996) produced grids on projections of panels of a cube encompassing the sphere. RPM equivalently use a projection from a cube contained within the sphere, referring to the grid as an "expanded cube". In this report, a C_N grid will refer to a conformal cubic grid having $N \times N$ points on each panel. For example, Fig. 1 shows a view from infinity of a C20 conformal-cubic grid, possessing $6 \times 20 \times 20$ grid points. Figure 2 shows the same conformal-cubic grid, but displayed on a longitude-latitude projection.

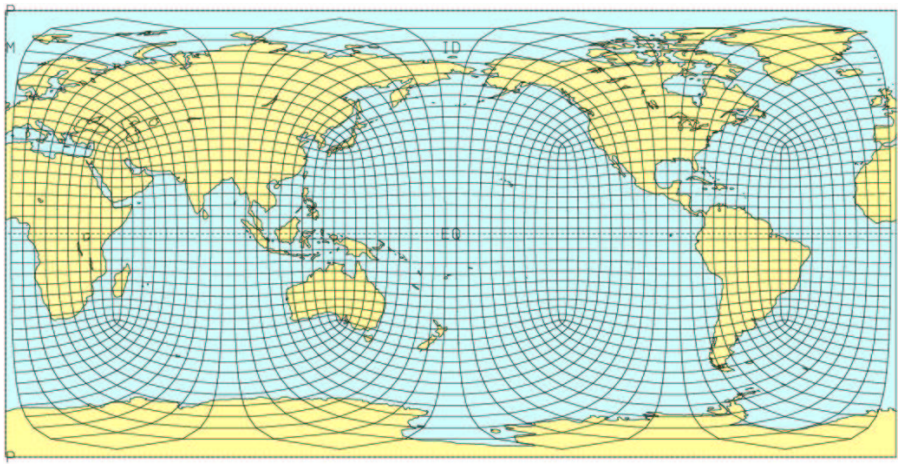

Figure 2: The same C20 conformal-cubic grid as in Fig. 1, but displayed on a longitude-latitude projection.

The development of C-CAM effectively began in 1994, with advection tests on the gnomonic cubic grid, as documented later by M97. This work was described at the André Robert Memorial Symposium, held in Montreal in October, 1994, at which the author learnt of the newly-devised C-C grid. This was soon followed by semi-Lagrangian advection tests on the C-C grid, described by McGregor (1996). A full primitive equations model was then developed, using aspects of the two-time-level semi-Lagangian framework previously developed for DARLAM, and also using its C-grid staggering for the winds; the first simulations, including physics packages, were described by McGregor and Dix (1997, 1998). About this time, in-house weather forecasts commenced at CAR using C-CAM (McGregor and Katzfey, 1998). This was followed by participation in the COMPARE III tropical cyclone intercomparison project (McGregor and Katzfey, 1999; Nagata et al., 2001). At about this time, the C-grid staggering was replaced by the reversible staggering scheme, documented by McGregor (2005). A description of the model as a general circulation model was provided by McGregor and Dix (2001). Consoldidation of the model dynamics and physics has actively continued, and the range of modelling activities has been extended to include trace gas modelling and a considerable number of regional climate simulations.

2 Coordinates and coordinate transformations

The radius of the Earth is denoted by R. (X, Y, Z) denotes the "physical" 3D Cartesian coordinates on the sphere, with Z pointing up through panel 1, normal to the Earth's surface. Each of (X, Y, Z) range between -R and R. In the case of using a stretched grid, the highest resolution panel will be panel 1.

The equations of motion will be written in terms of the 2D panel coordinates $(x,\ y,\ p)$ where p is a panel number $0 \leq p \leq 5$, and on each panel $0 \leq x \leq \pi R/2$. For $N \times N$ points on each panel, the x and y values are equally spaced at the average model grid resolution of

$$\Delta x \equiv \Delta y = 2\pi R/(4N); \tag{1}$$

this value can be determined by noting that four contiguous panels will go right around the globe. Values of x on each panel are given by $x_1 = \pi R/(4N)$, $x_2 = 3\pi R/(4N)$, ..., $x_N = (2N-1)\pi R/(4N)$, with corresponding values for y. Each grid point in $(x,\ y,\ p)$ space has an associated map factor, m, such that the physical spacing between grid points is $\Delta x/m$. The map factors vary from point to point. In the original C-C grid of Rancic et al. (1996), the map factors on any panel are equal to those in the corresponding position of any other panel; this property does not occur when using a stretched grid, with m being large on the finest-resolution panel and small on the coarsest resolution panel. Note that the grid is equally-spaced in terms of $(x,\ y)$ values, regardless of whether or not the grid is stretched.

For performing the grid calculations, it is necessary to relate the (X, Y, Z) grid values and map factors to those on the associated quasi-uniform 3D Cartesian (X', Y', Z') coordinates, also on the sphere. This is done by means of the Schmidt transformation.

2.1 The Schmidt transformation

This transformation was devised by Schmidt (1977). It is used to transform any orthogonal grid system on the sphere to a stretched version of the same grid, whilst preserving orthogonality and isotropy (provided that is the case for the original grid). The Schmidt magnification factor is here denoted by S; typical values are $S = 1$ (non-stretched), $S = 3$ (higher resolution over panel 1). In the C-CAM implementation of the Schmidt transformation, the (X, Y, Z) coordinate system is centred on panel 1. At the centre of the panel, the Z coordinate is directed upwards, while X and Y are directed south and east respectively. The Schmidt transformation acts to transform these Cartesian coordinate values and map factors as follows.

$$X = \frac{(1+\alpha)}{(1+\alpha Z'/R)}\frac{X'}{S}, \tag{2}$$

$$Y = \frac{(1+\alpha)}{(1+\alpha Z'/R)}\frac{Y'}{S}, \tag{3}$$

$$Z = \frac{\alpha R + Z'}{(1+\alpha Z'/R)}, \tag{4}$$

where α is zero for a non-stretched grid ($S = 1$); in general it is defined by

$$\alpha = \frac{S^2 - 1}{S^2 + 1}. \tag{5}$$

Note that the (x, y, p) values are unaffected by the Schmidt transformation, although the associated map factors are altered according to

$$m = \frac{(1 + \alpha Z^{'}/R)}{1 - \alpha} \frac{m^{'}}{S}. \tag{6}$$

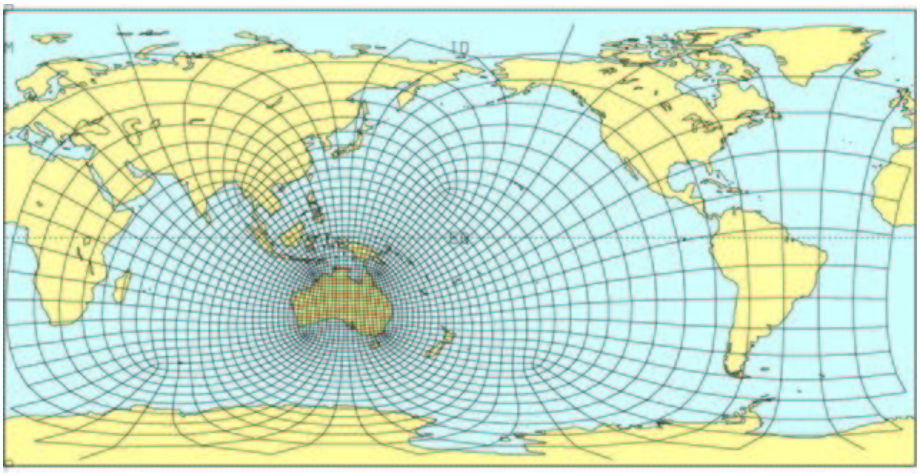

Figure 3: An example of a C20 conformal-cubic grid centred over Australia, with Schmidt magnification factor = 3.33.

At the centre of panel 1, where $Z = Z' = R$, (6) reduces to $m = Sm'$, verifying that the grid resolution on the (X, Y, Z) coordinates is magnified there by a factor S compared to the (X', Y', Z') coordinates. The non-stretched "equator" gets moved to $Z = \alpha R$, with a radius $(1+\alpha)R/S$. The transformations from the "physical" (X, Y, Z) coordinates to the associated quasi- regular-panel (X', Y', Z') are given by

$$X' = \frac{(1 - \alpha)}{(1 - \alpha Z/R)} SX, \tag{7}$$

$$Y' = \frac{(1 - \alpha)}{(1 - \alpha Z/R)} SY, \tag{8}$$

$$Z' = \frac{(Z - \alpha R)}{(1 - \alpha Z/R)}. \tag{9}$$

It can be seen from these equations that the "equator" in the stretched coordinates (i.e. $Z = 0$) is located at $Z' = -\alpha R$, where it has a radius $(1 - \alpha)SR$. Figure 3 shows an example of a stretched conformal-cubic grid.

2.2 Arrangement of the panels

A cube is constructed, encompassing the Earth and tangent to it for the associated (X', Y', Z') coordinates. Gnomonic projections (radially towards the centre of the Earth) are performed between the surface of the Earth and the surface of the cube. The following coordinates refer to the panels of the cube:

$(A,\ B,\ C)$: 3D Cartesian on the cube, with A, B and C pointing outwards through panels 0, 2 and 1 respectively;

$(a,\ b,\ p)$: 2D Cartesian on the panels of the cube.

Each of these coordinate values can range between -R and R , except that 0 $\leq p \leq 5$. Note that the $(x,\ y)$ coordinates on the sphere are orthogonal on each panel, although the projected $(a,\ b)$ coordinate lines on the faces of the cube are not orthogonal.

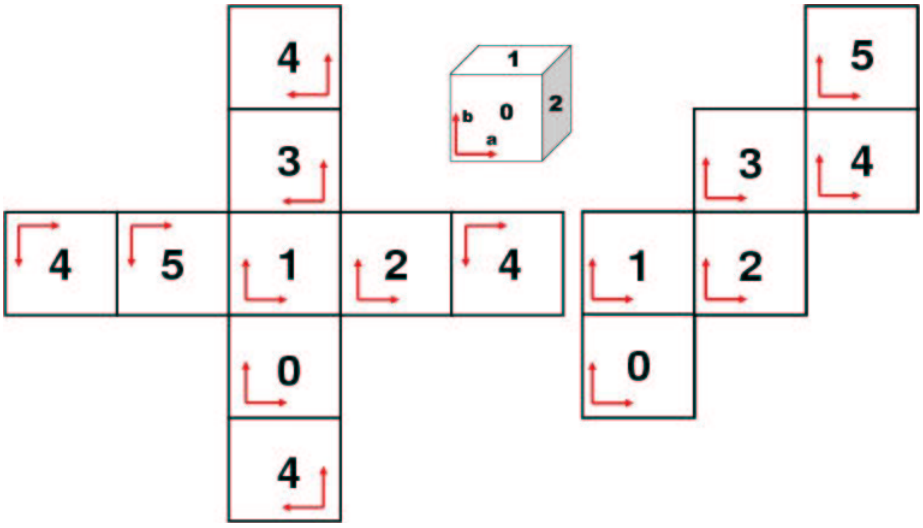

Figure 4: Layout of the panels and their relative orientation for three alternative, but equivalent, viewpoints.

The orientation of the panels and of the a and b axes (or, with the same orientations, the x and y axes) is given in Fig. 4. Each panel edge has N segments and each panel contains $N \times N$ quadrilateral elements. On each panel the range of a and b is -$R \leq a \leq R$, -$R \leq b \leq R$. The transformations between the (X, Y, Z), (A, B, C) and (a, b, p) representations are summarized in the following subsections.

Each C-CAM grid point is uniformly spaced in $(x,\ y)$ space; it has an associated (X, Y, Z) value and an associated (X', Y', Z') value, and that projection onto the cube has an associated (A, B, C) value, which corresponds simply to (a, b, p) values. The (a, b, p) representation is essentially required to calculate the grid indexing corresponding to values of (X, Y, Z).

2.2.1 Grid information supplied by the RPM routines

The RPM routines are used to produce (X', Y', Z') at grid points on panel 0 of the sphere. The corresponding $(a,\ b)$ on panel 0 of the cube are then calculated.

Values for (a, b) on the other panels follow easily from symmetry; these (a, b) are then projected back to give the remaining (X', Y', Z') on the sphere.

Non-integral grid values are needed only for determining the quadruple resolution grid used in the inverse index calculations described later. The quadruple resolution grid (needed only for one panel) is provided by the RPM algorithms using $4N$ points in each direction. Note that the grid points of the C_N grid align exactly with a subset of the higher-resolution (C_$4N$) grid.

2.2.2 Map factors, grid spacing and tangent vectors

The Rancic et al. (1996) routines are able to provide the m' map factors, which can be transformed by (6) to the final m values. In practice, for stretched grids, it has been found equally accurate (and possibly more self-consistent) to evaluate m as in McGregor (1997) by finite differencing of the neighbouring gridpoint Cartesian locations. Denoting the Cartesian position vector on the sphere by $\mathbf{r} \equiv (X, Y, Z)$, grid distances between adjacent grid points are calculated as

$$\left(\frac{\Delta x}{m}\right)_{i+1/2,j} = |\mathbf{r}_{i+1,j} - \mathbf{r}_{i,j}| \left(1 + \frac{|\mathbf{r}_{i+1,j} - \mathbf{r}_{i,j}|^2}{24}\right), \tag{10}$$

with a similar expression for each $(\Delta y/m)_{i,j+1/2}$. The multiplicative term is a correction for the curvature of the Earth. The final map factors at each grid point are evaluated by averaging the neighbour distances as follows

$$\left(\frac{\Delta x}{m}\right)_{i,j} = \left\{ \left(\frac{\Delta x}{m}\right)_{i-1/2,j} + \left(\frac{\Delta x}{m}\right)_{i+1/2,j} + \left(\frac{\Delta y}{m}\right)_{i,j-1/2} + \left(\frac{\Delta y}{m}\right)_{i,j+1/2} \right\}, \tag{11}$$

remembering that Δx and Δy are equal and satisfy (1).

For a C37 grid, the maximum grid length is midway along an edge and perpendicular to it (0.0818 R), while the minimum occurs at vertices (0.0262 R). The ratio of maximum-to-minimum grid length is 3.1; the corresponding ratio for the non-orthogonal McGregor (1997) grid is 2.1, whereas for a T42 Gaussian grid the ratio of maximum to minimum longitudinal grid increment is 26.8.

Unit tangential vectors aligned along the x and y axes are evaluated by finite differencing whilst setting up the grid at the beginning of simulations. It was considered worthwhile to make their determination as accurate as possible, as they correspond to the directions of the model wind components. The determination is illustrated for a typical grid point (i, j) in the interior of a panel. First-guess tangential vectors are calculated as

$$\mathbf{x}_{T0} = \mathbf{r}_{i+1,j} - \mathbf{r}_{i-1,j}, \quad \mathbf{y}_{T0} = \mathbf{r}_{i,j+1} - \mathbf{r}_{i,j-1}. \tag{12}$$

From these, two unit vectors are formed, actually tangential to the sphere

$$\hat{\mathbf{x}}_{T1} = \frac{\mathbf{y}_{T0} \times \mathbf{r}}{|\mathbf{y}_{T0} \times \mathbf{r}|}, \quad \hat{\mathbf{y}}_{T1} = \frac{\mathbf{r} \times \mathbf{x}_0}{|\mathbf{r} \times \mathbf{x}\mathbf{T}_{T0}|}. \tag{13}$$

In order to obtain orthogonal tangent vectors, new vectors are formed involving a small correction factor ϵ (yet to be determined)

$$\mathbf{x}_T = \hat{\mathbf{x}}_{T1} + \epsilon \hat{\mathbf{y}}_{T1}, \quad \mathbf{y}_T = \hat{\mathbf{y}}_{T1} + \epsilon \hat{\mathbf{x}}_{T1}. \tag{14}$$

Specifying that the dot product $\mathbf{x}_T \cdot \mathbf{y}_T$ should equal zero, readily yields

$$\epsilon = -\frac{\hat{\mathbf{x}}_{T1} \cdot \hat{\mathbf{y}}_{T1}}{1 + \sqrt{1 - (\hat{\mathbf{x}}_{T1} \cdot \hat{\mathbf{y}}_{T1})^2}}. \tag{15}$$

The final tangential vectors are

$$\hat{\mathbf{x}}_T = \frac{\mathbf{x}_T}{|\mathbf{x}_T|}, \quad \hat{\mathbf{y}}_T = \frac{\mathbf{y}_T}{|\mathbf{y}_T|}. \tag{16}$$

2.3 Transformations between the alternative coordinate representations

In the semi-Lagrangian solution of the primitive equations, it is necessary to calculate grid locations for an arbitrary (X, Y, Z). For this purpose, it is necessary to transform between the various coordinate representations on the sphere and projected cube. The various transformation are defined in the following subsections.

2.3.1 (X', Y', Z') on the sphere to (A, B, C) on the cube

$$(A, B, C) = \frac{(X', Y', Z')}{\max(|X'|, |Y'|, |Z'|)} R. \tag{17}$$

2.3.2 (A, B, C) on the cube to (X', Y', Z') on the sphere

$$(X', Y', Z') = \frac{(A, B, C)}{(A^2 + B^2 + C^2)^{1/2}} R. \tag{18}$$

2.3.3 (A, B, C) on the cube to (a, b, p) on the cube

This can be determined by the following six branching ("if") tests

$$\text{if } A = R \text{ then } p = 0,\ a = B,\ b = C; \tag{19}$$

$$\text{if } A = -R \text{ then } p = 3,\ a = -C,\ b = -B; \tag{20}$$

$$\text{if } B = R \text{ then } p = 2,\ a = -C,\ b = -A; \tag{21}$$

$$\text{if } B = -R \text{ then } p = 5,\ a = A,\ b = C; \tag{22}$$

$$\text{if } C = R \text{ then } p = 1,\ a = B,\ b = -A; \tag{23}$$

$$\text{if } C = -R \text{ then } p = 4,\ a = A,\ b = -B. \tag{24}$$

It can be verified by inspection that the following alternative equations produce equivalent results, but avoid the branching computations. The panel index, p, is given by

$$p = \max[A_{\text{int}}(3A_{int} - 3),\ B_{\text{int}}(7B_{\text{int}} - 3),\ C_{\text{int}}(5C_{\text{int}} - 3)]/2, \tag{25}$$

where

$$A_{int} = \text{int}\left(\frac{A}{R}\right),\ B_{int} = \text{int}\left(\frac{B}{R}\right),\ C_{int} = \text{int}\left(\frac{C}{R}\right) \tag{26}$$

and "int" indicates the truncated integer value. Note that (26) can only be used on computers where a floating point number divided by itself is exactly 1, i.e. where strict IEEE floating point behaviour is provided. The Cartesian coordinate position *(a, b, p)* on a panel of the cube is then

$$a = E_{p1}A + E_{p2}B + E_{p3}C \tag{27}$$

$$b = F_{p1}A + F_{p2}B + F_{p3}C, \tag{28}$$

where the nonzero members of matrices $\boldsymbol{E}$ and $\boldsymbol{F}$ are given by

$$E_{02} = E_{12} = -E_{23} = -E_{33} = E_{41} = E_{51} = F_{03}$$

$$= -F_{11} = -F_{21} = -F_{32} = -F_{42} = F_{53} = 1.$$

2.3.4 (a, b, p) on the cube to (A, B, C) on the cube

$$A = R,\ \ B = a,\ \ C = b \text{ for } p = 0, \tag{29}$$

$$A = -b,\ \ B = a,\ \ C = R \text{ for } p = 1, \tag{30}$$

$$A = -b,\ \ B = R,\ \ C = -a \text{ for } p = 2, \tag{31}$$

$$A = R, \;\; B = -b, \;\; C = -a \;\; \text{for } p = 3, \tag{32}$$

$$A = a, \;\; B = -b, \;\; C = -R \;\; \text{for } p = 4, \tag{33}$$

$$A = a, \;\; B = -R, \;\; C = b \;\; \text{for } p = 5. \tag{34}$$

2.3.5 (X, Y, Z) on the sphere to/from longitude-latitude

Denote longitude by λ and latitude by φ in polar coordinates. Denote unrotated Cartesian coordinates by $(\tilde{X}, \tilde{Y}, \tilde{Z})$ with $\tilde{Z}$ passing through the North pole and $\tilde{X}$ passing through the Equator at the Greenwich meridian. These can be converted to and from polar coordinates by

$$\tilde{X} = R \cos\lambda \sin\varphi, \tag{35}$$

$$\tilde{Y} = R \sin\lambda \sin\varphi, \tag{36}$$

$$\tilde{Z} = R \sin\varphi, \tag{37}$$

or, equivalently,

$$\lambda = \text{atan2}(\tilde{Y}, \tilde{X}) \;\; \text{with} \;\; -\pi \leq \lambda \leq \pi, \tag{38}$$

$$\varphi = \arcsin(\tilde{Z}/R), \tag{39}$$

The C-CAM grid is set up so that the Cartesian grid is located at (λ_0, φ_0) for $(X, Y, Z) = (0, 0, R)$. At (λ_0, φ_0) the X axis lies in a negative direction along $\lambda = \lambda_0$ and the Y axis lies along $\varphi = \varphi_0$. The coordinate rotation corresponds to rotating $(\tilde{X}, \tilde{Y}, \tilde{Z})$ by λ_0 and then by $-\varphi_0$. The rotated and unrotated Cartesian coordinates may be related as follows

$$\tilde{X} = \cos\lambda_0 \sin\varphi_0 X - \sin\lambda_0 Y + \cos\lambda_0 \cos\varphi_0 Z, \tag{40}$$

$$\tilde{Y} = \sin\lambda_0 \sin\varphi_0 X + \cos\lambda_0 Y + \sin\lambda_0 \cos\varphi_0 Z, \tag{41}$$

$$\tilde{Z} = -\cos\varphi_0 X + \sin\varphi_0 Z. \tag{42}$$

The above equations thus provide a means to convert values of (X, Y, Z) to corresponding values of $(\tilde{X}, \tilde{Y}, \tilde{Z})$ and thereby to values of (λ, φ), or vice versa.

2.3.6 Zonal and meridional wind components

These zonal and meridional wind components are not required within C-CAM itself, but conversions to those components are required for post-processing display purposes, and also for conversion of initial data to the model grid points. The conversions are most easily determined in terms of the model (rotated) 3D Cartesian coordinates. The unit vector for the physical north pole is given by

$$\hat{\mathbf{k}} = (-\cos\vartheta_0, 0, \sin\vartheta_0). \tag{43}$$

The unit vector along the zonal components is

$$\hat{\mathbf{n}}_{zon} = \frac{\hat{\mathbf{k}} \times \mathbf{r}}{|\hat{\mathbf{k}} \times \mathbf{r}|} = \frac{(-\sin\vartheta_0 Y, \sin\vartheta_0 X + \cos\vartheta_0 Z, -\cos\vartheta_0 Y)}{\sqrt{\sin^2\vartheta_0 X^2 + Y^2 + \cos^2\vartheta_0 Z^2}}. \tag{44}$$

The meridional unit vector is not explicitly needed. For completeness, it is

$$\hat{\mathbf{n}}_{mer} = \frac{\mathbf{r} \times \hat{\mathbf{n}}_{zon}}{|\mathbf{r} \times \hat{\mathbf{n}}_{zon}|} = \frac{(-\sin\vartheta_0 Y, \sin\vartheta_0 X + \cos\vartheta_0 Z, -\cos\vartheta_0 Y)}{\sqrt{\sin^2\vartheta_0 X^2 + Y^2 + \cos^2\vartheta_0 Z^2}}. \tag{45}$$

Now let Θ denote the (anticlockwise) angle of $\hat{\mathbf{x}}_T$ from $\hat{\mathbf{n}}_{zon}$. $\hat{\mathbf{x}}_T$ is the unit vector along the model x coordinate, given by (16). Θ is given by

$$\cos\Theta = \hat{\mathbf{n}}_{zon} \cdot \hat{\mathbf{x}}_T; \ \sin\Theta = \hat{\mathbf{n}}_{zon} \cdot \hat{\mathbf{y}}_T. \tag{46}$$

Writing u and v as the wind components in the model coordinates, the final transformations are thus given by

$$u_{zon} = u\cos\Theta - v\sin\Theta, \quad v_{mer} = u\sin\Theta + v\cos\Theta, \tag{47}$$

or, conversely,

$$u = u_{zon}\cos\Theta + v_{mer}\sin\Theta, \ \ v = -u_{zon}\sin\Theta + v_{mer}\cos\Theta. \tag{48}$$

2.4 Procedure for setting up a C-CAM grid

The above equations provide the information needed to set up a stretched C-CAM grid.

1. Choose the location for the centre of the highest resolution panel 1, in terms of longitude and latitude, (λ_0, φ_0).

2. Choose the desired grid length for that panel.

3. Choose suitable values of N and S to provide that resolution.

4. Use the RPM routines to provide (*X', Y', Z'*) for a C-CAM grid with panel 1 centred at (λ_0, φ_0).

5. Use the Schmidt transformation equations (2) to (6) to provide (*X, Y, Z*) for the final grid system.

2.5 Inverse calculation of grid coordinates from (X, Y, Z)

The semi-Lagrangian advection procedure to be described in Section 3 produces departure points on the sphere in terms of the 3D Cartesian coordinates (X, Y, Z). Subsequent interpolations to obtain field values require those departure points to be expressed in terms of indices and panel numbers. This is most readily determined by calculations projected onto the faces of the cube, where the number of spatial dimensions has been reduced from three to two. Note that indices and panel numbers on the sphere are identical to those of the projected point on the cube.

The non-orthogonal grid used by M97 provides analytic expressions for the grid indices given these (a, b) values on the cube. Such expressions are not available in (a, b) space for the RPM grid; it appeared initially that this could inhibit the use of semi-Lagrangian methods on this grid. However, as described below, a technique has been devised whereby the indices are determined by simple iterations (two iterations in practice) performed on the faces of the cube using a quadruple-resolution grid. For this iterative calculation, the quadruple-resolution grid performed more accurately than a double-resolution grid. An eight-times resolution grid produced no extra benefits. Note that the computation time for this inverse calculation is independent of the resolution of the iterative grid.

2.6 Inverse index determination on a panel

The description here is given in terms of the quadruple-resolution grid. Given the projected values $(a,\ b)$ on a known panel of the cube, we wish to find the position on the panel in terms of index values $(I,\ J)$ where I and J need not be integers but satisfy $1 \le I < 4N+1$ and $1 \le J < 4N+1$. Note that when I and J both have integer values, the corresponding (a, b) coincides with a grid point.

An iterative grid point near $(I,\ J)$ is denoted by $(i,\ j)$; the area surrounding it is divided into four quadrants. In "northeast" quadrants (valid for the triangular region $0 \le I - i \le 1$, $0 \le J - j < I - i$) simple bilinear interpolation gives for the a-component

$$a = a_{i,j} + (I - i)(a_{i+1,j} - a_{i,j}) + (J - j)(a_{i,j+1} - a_{i,j}). \tag{49}$$

This formula can be generalized to cover all four quadrants

$$a = a_{i,j} + i^{'}(I - i)(a_{i+i^{'},j} - a_{i,j}) + j^{'}(J - j)(a_{i,j+j^{'}} - a_{i,j}), \tag{50}$$

where the desired quadrant is selected as described below by allocating particular values to the sign functions $i^{'} = \pm 1, j^{'} = \pm 1$. The corresponding expression for the b-component is

$$b = b_{i,j} + i^{'}(I - i)(b_{i+i^{'},j} - b_{i,j}) + j^{'}(J - j)(b_{i,j+j^{'}} - b_{i,j}). \tag{51}$$

The iterative solution proceeds in the following manner. A first guess is denoted by $(I_0, J_0) = (1 + 2N + 2Na/R,\ 1 + 2N + 2Nb/R)$. The quadrant is selected from the previous guess (I_0, J_0) with

$$i^{'} = \mathrm{sign}(1, I_0 - i),\ j^{'} = \mathrm{sign}(1, J_0 - j), \tag{52}$$

where

$$i = \text{nint}(I_0),\ j = \text{nint}(J_0), \tag{53}$$

and where "sign" and "nint" refer to the standard Fortran functions. Writing

$$\delta_a a = a_{i+i',j} - a_{i,j};\ \ \delta_b a = a_{i,j+j'} - a_{i,j}, \tag{54}$$

$$\delta_a b = b_{i+i',j} - b_{i,j};\ \ \delta_b b = b_{i,j+j'} - b_{i,j}, \tag{55}$$

the next iteration gives the following non-integer I and J values

$$I = i + \frac{(a - a_{i,j})\delta_b b - (b - b_{i,j})\delta_a a}{i'(\delta_a a \delta_b b - \delta_b a \delta_a b)}, \tag{56}$$

and

$$J = j + \frac{(b - b)\delta_b a - (a - a_{i,j})\delta_a b}{j'(\delta_a a \delta_b b - \delta_b a \delta_a b)}. \tag{57}$$

Equations (52) - (57) are repeated until convergence is achieved (two iterations in practice).

The above equations refer to the quadruple-resolution grid. These I and J are simply converted to regular grid values

$$I_{\text{regular}} = \frac{I+3}{4},\ \ J_{\text{regular}} = \frac{J+3}{4}. \tag{58}$$

3 Horizontal advection and interpolation on the conformal-cubic grid

Horizontal advection on the sphere of a scalar field ξ may be written as

$$\frac{d\xi}{dt} = 0, \tag{59}$$

where

$$\frac{d}{dt} = \frac{\partial}{\partial t} + mu\frac{\partial}{\partial x} + mv\frac{\partial}{\partial y} \tag{60}$$

and where $u \equiv m^{-1}(dx/dt)$ and $v \equiv m^{-1}(dy/dt)$ are the physical velocity components along the x and y coordinates. The two-time-level semi-Lagrangian solution at a new time step is

$$\xi^{\tau+1} = \xi^{\tau *}, \tag{61}$$

where $\xi^{\tau *}$ is the value of ξ evaluated by interpolation at the upstream departure point at time τ.

3.1 Derivation of departure points - method 1

Following McGregor (1993) the departure points of the 3D grid point located at $\mathbf{r}^{\tau+1}$ can be written in terms of the truncated Taylor series of the total derivatives

$$\mathbf{r}^{\tau} \approx \mathbf{r}^{\tau+1} + \sum_{n=1}^{3} \frac{(-\Delta t)^n}{n!} \frac{d^n \mathbf{r}^{\tau+1}}{dt^n}, \tag{62}$$

where

$$\frac{d^n \mathbf{r}(t)}{dt^n} = \frac{d}{dt}\left[\frac{d^{n-1}\mathbf{r}(t)}{dt^{n-1}}\right] \quad n = 2, 3. \tag{63}$$

The solution is second-order accurate in time provided that d/dt is evaluated using (60) without the partial time derivative term, but with velocities centred at time $\tau+1/2$. These velocities are usually determined by an extrapolation formula with third-order accuracy in time, as suggested by Temperton and Staniforth (1987),

$$\mathbf{u}^{\tau+1/2} = (15\mathbf{u}^{\tau} - 10\mathbf{u}^{\tau-1} + 3\mathbf{u}^{\tau-2})/8. \tag{64}$$

As in M97, the higher material derivatives in (62) are evaluated by application of (60) with simple centred finite differences. For the first term of the Taylor series in (62), the 3D Cartesian velocity components are used directly. This produces greater accuracy for the C-CAM grid than using a finite difference version of (60) to evaluate this term.

Equation (62) is applied separately to each Cartesian component in the form (*X, Y, Z*) to give corresponding departure point values; the two-iteration inverse procedure of section 2 then gives the equivalent departure points in terms of (*i, j, p*) where i and j are non-integral grid indices. As in M97, the use of Cartesian components allows the determination of departure points to pass over panel boundaries in a transparent manner. Some extra economy in the computations may be achieved by first normalizing the velocity components u and v to units of grid point per time step. Further details of this approach are provided by McGregor (1996).

3.2 Derivation of departure points - method 2

The following method is presently used. The velocity at the arrival point may be written in Cartesian vector form as

$$\mathbf{u} = u\hat{\mathbf{x}}_T + v\hat{\mathbf{y}}_T, \tag{65}$$

where the unit tangent vectors are given by (16) and the velocities are centred at time-level $\tau + 1/2$, as in the previous subsection. The departure point of the 3D grid point located at $\mathbf{r}^{\tau+1}$ is given as first guess by

$$\mathbf{r}_1^{\tau} = \mathbf{r}^{\tau+1} - \mathbf{u}(\mathbf{r}^{\tau+1})\Delta t \tag{66}$$

The $\mathbf{r}_1^{\tau}$ grid location is transformed by the methods described in Section 2 to a value of (x, y, p); bi-cubic interpolation of $\mathbf{u}$ is then used on the panels (as

described in the next subsection) to determine separately the three Cartesian wind components, and thus $\mathbf{u}(\mathbf{r}_1^\tau)$. The second-guess departure point is then defined as

$$\mathbf{r}_2^\tau = \mathbf{r}^{\tau+1} - \left(\mathbf{u}(\mathbf{r}^{\tau+1}) + \mathbf{u}(\mathbf{r}_1^\tau)\right) \Delta t/2. \tag{67}$$

This procedure is repeated one more time to give $\mathbf{u}(\mathbf{r}_2^\tau)$, and the final departure point is taken as

$$\mathbf{r}^\tau = \mathbf{r}^{\tau+1} - \left(\mathbf{u}(\mathbf{r}^{\tau+1}) + \mathbf{u}(\mathbf{r}_2^\tau)\right) \Delta t/2. \tag{68}$$

3.3 Interpolation of field values

During an advective calculation, the values (i, j, p) are used to determine the value of the advected ϕ field via quasi-bicubic interpolation centred on a 4×4 stencil. Quasi-cubic interpolation was suggested by Philippe Courtier; it is used in the operational ECMWF model and is described by Ritchie et al. (1995). During the first direction of interpolation, linear interpolations are performed along the edges of the 4×4 stencil. This reduces the stencil to 12 points, but maintains high accuracy.

During even time steps, $x-y$ interpolation is performed (x interpolation before y interpolation); during odd time steps $y-x$ interpolation is performed. Analogously to the splitting methods of Marchuk (1974), this alternation should produce some reduction in truncation errors. The advection tests are found to be quite insensitive to the starting order of the alternating interpolations; some sensitivity is found if only non-alternating interpolation is used. Prior to performing the interpolations, data is extended on each of the 6 panels by two rows/columns in each direction. Near the vertices, the points used in the extension depend on whether the array is to be used for $x-y$ or $y-x$ interpolation. The nature of the extension is illustrated for panel 0 (following the panel notation of 4) of a C5 grid, shown for both types of interpolation in Figs. 5 and 6. It may be seen from these Figures that the interpolation stencil reduces to either 9 or 11 independent points near the vertices.

	45_5	12_1	22_1	32_1	42_1	52_1	12_2	
54_5	55_5	11_1	21_1	31_1	41_1	51_1	11_2	21_2
45_5	55_5	15_0	25_0	35_0	45_0	55_0	11_2	12_2
44_5	54_5	14_0	24_0	34_0	44_0	54_0	21_2	22_2
43_5	53_5	13_0	23_0	33_0	43_0	53_0	31_2	32_2
42_5	52_5	12_0	22_0	32_0	42_0	52_0	41_2	42_2
41_5	51_5	11_0	21_0	31_0	41_0	51_0	51_2	52_2
52_5	51_5	55_4	54_4	53_4	52_4	51_4	51_2	41_2
	41_5	45_4	44_4	43_4	42_4	41_4	52_2	

Figure 5: Illustration of extension of C5 array for x-y interpolation on panel 0. Grid points are indicated by ij_n, where n denotes the panel number.

It should be mentioned that the interpolations on the non-orthogonal grids of M97 were performed wholly within panels and thus near the panel edges the

interpolations were not centred on the 4×4 stencils. It was noted in that paper that the uncentred locations might occasionally lead to weak instabilities near the panel edges in a full primitive equations model. The present scheme always uses centred stencils, avoiding such an eventuality.

	21_1	12_1	22_1	32_1	42_1	52_1	41_1	
12_1	11_1	11_1	21_1	31_1	41_1	51_1	51_1	52_1
45_5	55_5	15_0	25_0	35_0	45_0	55_0	11_2	12_2
44_5	54_5	14_0	24_0	34_0	44_0	54_0	21_2	22_2
43_5	53_5	13_0	23_0	33_0	43_0	53_0	31_2	32_2
42_5	52_5	12_0	22_0	32_0	42_0	52_0	41_2	42_2
41_5	51_5	11_0	21_0	31_0	41_0	51_0	51_2	52_2
45_4	55_4	55_4	54_4	53_4	52_4	51_4	51_4	41_4
	54_4	45_4	44_4	43_4	42_4	41_4	52_4	

Figure 6: Illustration of extension of C5 array for y-x interpolation on panel 0.

3.4 Some comments on geometric and horizontal advection aspects

A semi-Lagrangian advection scheme has been here described for the conformal-cubic grid of Rancic et al. (1996). The grid has quasi-uniform resolution, although it is not as uniform as the non-orthogonal cubic grids studied by M97. In advection tests shown by McGregor (1996), the conformal grid performed most accurately overall, being superior to the M97 scheme, and better still than tests on the Gaussian longitude-latitude grid. Tests with a coarser conformal-cubic grid produced similar or better accuracy than semi-Lagrangian tests on a reduced Gaussian grid having a similar number of grid points.

The conformal scheme is slightly more expensive than the non-orthogonal M97 scheme; instead of an analytic formula, it requires two iterations to determine the departure points in terms of panel indices. However, the conformal scheme has the advantage of always being able to use a centred interpolation stencil. It is also well suited to quasi-cubic interpolation. The semi-Lagrangian advection schemes on the cubic grids are efficient and run only 10%-20% slower than on a Gaussian grid having a similar number of points. The reduced Gaussian grid requires extra interpolations and runs at a quite similar speed to the cubic grids.

Although the vertices of the grid represent singularities (meeting at 120^o instead of being orthogonal), they are easily handled in the finite-difference scheme. No disruption was found for patterns being advected over the vertices, quite unlike the situation for advection over the poles of a Gaussian grid.

4 Reversible staggering of the winds

In meteorological modeling, there are several common grid arrangements for horizontally staggering the wind components relative to the mass variables. The various grids produce different behavior for geostrophic adjustment, as first clarified by Winninghoff (1968). A summary of his work, as well as a nomenclature for these common meteorological grids, was provided by Arakawa and Lamb (1977). The staggered C grid is rather popular for atmospheric models. The main reason for its popularity is that it has good dispersion behavior for large Rossby radius of deformation (defined relative to the grid spacing).

However, for small radius of deformation the C grid has poor dispersion behavior, which has resulted in greater popularity of the B grid for ocean models (e.g. Randall, 1994). Randall (1994) went on to advocate the Z grid where divergence and vorticity are the primary variables, both stored on an unstaggered grid. He showed that this arrangement has superior dispersion properties for both large and small Rossby radii of deformation. The reversible staggering arrangement proposed in this paper is denoted as the R grid; it is based on the wind components, but produces dispersion behavior that is generally very similar to that of the Z grid.

Unstaggered grids are appealing in that they allow the various physical parameterizations to be carried out at coincident points. An additional appeal for semi-Lagrangian models is that one set of trajectories can be used to provide common departure points for all variables. Unfortunately, the simple unstaggered A grid has quite poor dispersion properties. It also decouples into four separate families of solutions for the gravity waves (e.g. McGregor and Leslie, 1977) and therefore usually requires horizontal filtering of the solutions. This decoupling problem does not occur with the staggered C grid, but it does occur to a lesser extent for the B grid. The R grid does not experience this decoupling of solutions.

Consider now a formulation of the primitive equations where all primary variables are stored on the A grid, with all physical processes and advection calculated on the A grid, but with a transformation made to the C grid for calculation of the gravity wave terms. If this staggering is done by a simple linear averaging of the wind components, the overall scheme still has the same dispersion behavior as the usual A grid scheme. On the other hand, the reversible staggering procedure presented here as the R grid scheme maintains the convenience of the A grid during most calculations, but produces superior gravity wave dispersion characteristics.

Figure 7: Relative location of unstaggered (|) and staggered (×) grid points, and "pivot" points (⋆).

The new reversible interpolation schemes is derived by considering interpolation to the "pivot" points illustrated in Fig. 7. The unstaggered x velocity

components are denoted by U_m and the staggered components by $u_{m+\frac{1}{2}}$. Equating the representations of U and u at the "pivot" point $x_{m+\frac{3}{4}}$ gives for the "left" transformation to u (or the "right" transformation back to U) the following spatially implicit "compact" 3-point formula for the common interpolated velocity component at $x_{m+\frac{3}{4}}$:

$$\frac{u_{m-\frac{1}{2}} + 10u_{m+\frac{1}{2}} + 5u_{m+\frac{3}{2}}}{16} = \frac{5U_m + 10U_{m+1} + U_{m+2}}{16} \tag{69}$$

This new interpolation formulae has been derived by the generalized Vandermonde method. The author is grateful to Jim Purser for suggesting use of the Vandermonde method, which is more accurate than an earlier implementation derived from Lagrange interpolation. As may be verified by substitution, (69) is designed to produce a common value at the pivot points for polynomials up to order 4, although the common value only exactly fits a first-order polynomial. Using symmetry, one can easily write analogous formulae for the alternative "right" transformation, based on the "pivot" point $x_{m+\frac{1}{4}}$.

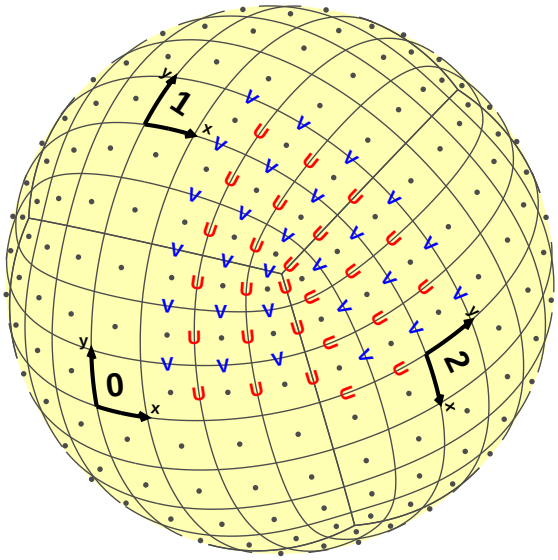

Figure 8: View of the C-CAM grid showing the winds in their staggered locations, illustrated for a C9 grid.

Although it is intended that the staggering interpolation formula (69) will be used for real variables in meteorological applications, it can also be applied to complex variables. It is instructive to consider the case of a unit amplitude Fourier component with $U = e^{ix\theta/d}$, where d denotes the grid spacing, the wavelength is Md, and $\theta = 2\pi/M$. If the unstaggered grid points are located at $x = md$, then $U_m = e^{im\theta}$. It can be verified by substitution into (69) that the corresponding staggered variables satisfy

$$u_{m+\frac{1}{2}} = e^{i(m+1)\theta}\frac{\left(e^{i\theta} + 10 + 5e^{-i\theta}\right)}{\left(e^{-i\theta} + 10 + 5e^{i\theta}\right)} \equiv e^{i(m+\frac{1}{2})\theta}e^{i\phi(\theta)} \quad \text{say.} \tag{70}$$

Because the denominator of (70) is the complex conjugate of the numerator, $u_{m+\frac{1}{2}}$ must also have unit magnitude. This establishes the important property that the Fourier components are transformed unchanged in amplitude, undergoing only a phase shift. The expression $\phi(\theta)$ in (70) gives the phase shift of each Fourier component. For the "left" transformation scheme (69), ϕ is always positive, corresponding to a (usually small) left-ward displacement.

The relative locations of the staggered wind components on the C-CAM grid are illustrated in Fig. 8. Details of the dispersion properties of the reversible staggering procedure are provided by McGregor (2005), as well as some alternative versions of the scheme.

4.1 Numerical evaluation of the staggering transformations

The staggering-unstaggering equation (69) forms a linear system that may be solved as a matrix inversion problem. The dominant terms (for a periodic domain) are

$$u_{m+\frac{1}{2}} = 0.03U_{m-1} + 0.26U_m + 0.93U_{m+1} - 0.25U_{m+2}$$

$$+0.04U_{m+3} - 0.01U_{m+4}, \tag{71}$$

While this series expression is useful for illustrating the nature of the solutions, it converges too slowly to be recommended. Accurate and efficient evaluation may be obtained by use of a tridiagonal solver. The periodic nature of the conformal-cubic grid requires a cyclic tridiagonal solver, such as described by Temperton (1975).

Alternatively, it is straightforward to devise an efficient iterative solution to (69). First, the equation is combined with itself to bring out a diagonal dominance; multiplying (69) by 32 and subtracting 16 times (69) evaluated for $m+1$ gives

$$2u_{m-\frac{1}{2}} + 19u_{m+\frac{1}{2}} - 5u_{m+\frac{5}{2}} = 10U_m + 15U_{m+1} - 8U_{m+2} - U_{m+3}. \tag{72}$$

Given values for the unstaggered U, (72) suggests the following iterative solution

First guess:

$$u^0_{m+1/2} = \left(10U_m + 15U_{m+1} - 8U_{m+2} - U_{m+3}\right)/19; \tag{73}$$

Later iterations:

$$u^n_{m+1/2} = u^0_{m+1/2} - \frac{2u^{n-1}_{m-1/2}}{19} + \frac{5u^{n-1}_{m+5/2}}{19}. \tag{74}$$

Four iterations are found to give good convergence. The corresponding formulae for unstaggering may be written in the obvious manner.

5 Vertical advection

5.1 Choice of sigma levels

Two families of vertical sigma levels are available, both being extensions of the early cubic formula given by Smagorinsky et al. (1965), providing symmetric definitions above and below $\sigma_K = 0.5$ (i.e. $\sigma_1 = 1 - \sigma_K$, and so on). For each family, the number of vertical levels, K, is specified in advance.

Family A1

This family is compatible with the levels used in the CSIRO Mk2 and Mk3 models; those models are described respectively by McGregor et al. (1993) and Gordon et al. (2002). This family locates the full-levels midway between the half-levels (the Mk2 and Mk3 models have this requirement for energy conservation reasons that do not apply to C-CAM). The simple version of this specification is

$$\sigma_{k+\frac{1}{2}} = (1 - k/K)^2(1 + 2k/K) \text{ for } k = 0, 1, 2, .., K \tag{75}$$

with averaging to give full-level values as

$$\sigma_k = (\sigma_{k-\frac{1}{2}} + \sigma_{k+\frac{1}{2}})/2 \text{ for } k = 1, 2, .., K \tag{76}$$

Family A2

This is a modification of family A2, also compatible with the Mk2 and Mk3 levels, but with the uppermost sigma level, σ_K, also specified. A quantity $\hat{\alpha}$ is calculated

$$\hat{\alpha} = \frac{[1 - 4\sigma_K - (1 - 2/K)^3]}{[1 - 2/K - (1 - 2/K)^3]}, \tag{77}$$

providing the following values,

$$2\sigma_{k+.5} = 1 + \hat{\alpha}(1 - 2k/K) + (1 - \hat{\alpha})(1 - 2k/K)^3 \text{ for } k = 0, 1, 2, .., K. \tag{78}$$

The full-level values again satisfy (76).

Family B

This is a formula which is valid for both full- and half-levels, and thus provides a smoother transition between full- and half-level values. Essentially the formula is a linear combination of the original formula of Smagorinsky et al. (1965) and an equally-spaced specification of the levels. To determine the linear weighting, the uppermost sigma level, σ_K, is again specified. A suitable weight is now given by

$$\hat{\alpha} = \frac{2K^2(2\sigma_K - 1)}{(4K^2 - 1)} \tag{79}$$

so that

$$\sigma_{k+\frac{1}{2}} = \hat{\alpha}(1-k/K)^2(1+2k/K) + (1-\hat{\alpha})(1-k/K) \text{ for } k = 0, \frac{1}{2}, 1, \frac{3}{2}, 2, .., K. \tag{80}$$

5.2 The TVD vertical advection scheme

C-CAM uses the total variation diminishing (TVD) method for vertical advection, as advocated by Thuburn (1993). Treating the vertical advection equation in split form, it may be written as

$$\frac{\partial q}{\partial t} + \dot{\sigma}\frac{\partial q}{\partial \sigma} \equiv \frac{\partial q}{\partial t} + \frac{\partial \dot{\sigma} q}{\partial \sigma} - q\frac{\partial \dot{\sigma}}{\partial \sigma} = 0, \tag{81}$$

using water vapour mixing ratio, q, as an example here. Following Thuburn (1993), this equation is further split, into the following two sequentially-solved equations

$$\frac{\partial q}{\partial t} + \frac{\partial \dot{\sigma} q}{\partial \sigma} = 0 \tag{82}$$

and

$$\frac{\partial q}{\partial t} - q\frac{\partial \dot{\sigma}}{\partial \sigma} = 0. \tag{83}$$

Equation (82) is solved using the flux-based TVD scheme. Low- and high-order fluxes are defined at the half-levels as follows. Noting that $\dot{\sigma}$ is positive downwards, the low-order flux is the first-order upstream expression

$$F^L_{k+1/2} = \frac{\dot{\sigma}_{k+1/2}}{2}(q_k + q_{k+1}) - \frac{|\dot{\sigma}_{k+1/2}|}{2}(q_k - q_{k+1}). \tag{84}$$

The following high-order flux is used, based on the Lax-Wendroff method

$$F^H_{k+1/2} = \frac{\dot{\sigma}_{k+1/2}}{2}\frac{(\sigma_{k+1}q_k + \sigma_k q_{k+1})}{(\sigma_{k+1} + \sigma_k)} - \frac{\dot{\sigma}^2_{k+1/2}\Delta t}{2}\frac{(q_{k+1} - q_k)}{(\sigma_{k+1} - \sigma_k)}. \tag{85}$$

This expression corresponds to a weighted average at the half-level, but modified by a half timestep's worth of advection. In the TVD method, these fluxes are combined using a flux-limiter, C, such that the net flux F is given by

$$F_{k+1/2} = F^L_{k+1/2} + C_{k+1/2}\left(F^H_{k+1/2} - F^L_{k+1/2}\right). \tag{86}$$

The C-CAM code provides options for three alternative flux limiters:

a) the original Van Leer (1974) flux-limiter

$$C_{k+1/2} = \frac{r_{k+1/2} + |r_{k+1/2}|}{1 + |r_{k+1/2}|}, \tag{87}$$

b) the "MC" (monotonized centred) flux-limiter of Van Leer (1977)

$$C_{k+1/2} = \max\left[0, \min\left(2r_{k+1/2}, \frac{1+r_{k+1/2}}{2}, 2\right)\right], \tag{88}$$

c) the "superbee" flux limiter of Roe (1985)

$$C_{k+1/2} = \max\left[0, \min\left(1, 2r_{k+1/2}\right), \min\left(2, r_{k+1/2}\right)\right]. \tag{89}$$

In each of these formulae, the smoothness variable $r_{k+1/2}$ is given by

$$r_{k+1/2} = \frac{q_k - q_{k-1}}{q_{k+1} - q_k} \text{ for } \dot{\sigma} < 0, \tag{90}$$

$$r_{k+1/2} = \frac{q_{k+2} - q_{k+1}}{q_{k+1} - q_k} \text{ for } \dot{\sigma} > 0; \tag{91}$$

it represents the ratio of the slope of the solution upstream of $k + 1/2$ to the slope of the solution across the interface at $k + 1/2$ itself; r is approximately unity where the numerical solution is smooth (Durran, 1999), so the flux will then be weighted towards the higher-order expression; r negative when there is a local maximum or minimum immediately upstream of $k + 1/2$, in which case $C_{k+1/2}$ becomes zero and the low-order flux is used. The behaviour of the TVD scheme is described by Durran (1999) and the various flux-limiters compared; he indicates a preference for the "MC" limiter. In C-CAM, the "superbee" flux limiter is usually used, although the other forms are found to give fairly similar results. The final solution to (82) is given by

$$q_k^{\tau+1} = q_k^{\tau} - \frac{F_{k+1/2} - F_{k-1/2}}{\sigma_{k+1/2} - \sigma_{k-1/2}}, \tag{92}$$

where values at the current time step are denoted by superscript τ and those at the subsequent time step by $\tau + 1$

After solving (82) by TVD methods, (83) is solved using simple explicit (forward-in-time) differencing; an alternative implicit treatment is available for (83), but little sensitivity is found to the method of solution of this equation.

In the C-CAM model, vertical advection is performed both before and after the "dynamics", each time for a time increment of $\Delta t/2$, in order to reduce time truncation errors related to time-splitting. To guard against the possibility of computational instability during vertical advection, the maximum Courant number for vertical advection is calculated each time step, and if it ever exceeds 1, then the vertical advection is multiply performed with a suitably subdivided time increment for that time step.

6 The primitive equations in continuous form

The 2D material time derivative is defined as

$$\frac{d_H}{dt} = \frac{\partial}{\partial t} + mu\frac{\partial}{\partial x} + mv\frac{\partial}{\partial y}, \tag{93}$$

where m denotes the map factor of the conformal projection. Where p_s is the surface pressure, the primitive equations for terrain-following σ coordinates, ($\sigma = p/p_s$), may then be written in the following form:

Horizontal momentum

$$\frac{d_H u}{dt} + m\frac{\partial \phi_v}{\partial x} + mR_d T_v \frac{\partial \ln p_s}{\partial x} + \dot{\sigma}\frac{\partial u}{\partial \sigma} = (f + f_m)v + \tilde{N}_u \tag{94}$$

$$\frac{d_H v}{dt} + m\frac{\partial \phi_v}{\partial y} + mR_d T_v \frac{\partial \ln p_s}{\partial y} + \dot{\sigma}\frac{\partial v}{\partial \sigma} = -(f + f_m)u + \tilde{N}_v, \tag{95}$$

where ϕ_v is the geopotential (including virtual temperature contributions) and f is the Coriolis parameter; R_d is the gas constant for dry air. T_v is the virtual temperature defined by

$$T_v = T\left[1 + \left(\frac{R_v}{R_d} - 1\right)q\right] \tag{96}$$

where T is temperature and R_v is the gas constant for water vapour; q is the mixing ratio of water vapour. The various $\tilde{N}$ terms denote possible contributions from physical parameterizations. The extra map projection terms f_m are rather small and are given by

$$f_m = u\frac{\partial m}{\partial y} - v\frac{\partial m}{\partial x}. \tag{97}$$

Temperature

$$\frac{d_H T}{dt} + \dot{\sigma}\frac{\partial T}{\partial \sigma} - \frac{R_d T}{c_p \sigma}\frac{\omega}{p_s} = \tilde{N}_T, \tag{98}$$

where c_p is the specific heat of water vapour at constant pressure and ω is the pressure vertical velocity.

Moisture

$$\frac{d_H q}{dt} + \dot{\sigma}\frac{\partial q}{\partial \sigma} = \tilde{N}_q. \tag{99}$$

Continuity

$$\frac{d_H \ln p_s}{dt} + D + \frac{\partial \dot{\sigma}}{\partial \sigma} = 0, \tag{100}$$

where the divergence D is given by

$$D = m^2\left\{\frac{\partial (u/m)}{\partial x} + \frac{\partial (v/m)}{\partial y}\right\}. \tag{101}$$

Hydrostatic equation

$$\frac{\partial \phi_v}{\partial \sigma} = -\frac{R_d T_v}{\sigma}, \tag{102}$$

6.1 Continuity equation and diagnostic equations for vertical velocity

For a K-level model, the above continuity equation (100) consists of K equations. It provides the time variation of p_s and diagnoses the (K-1) half-level values of the staggered vertical velocity variable. It is convenient to rewrite (100) as

$$\frac{\partial \ln p_s}{\partial t} + D + \frac{\partial \dot{\sigma}}{\partial \sigma} = N_{p_s}, \tag{103}$$

where N_{p_s}, denoting the advective time rate of change of $\ln p_s$, is formally defined by

$$N_{p_s} = -\mathbf{u} \cdot \nabla \ln p_s = -mu\frac{\partial \ln p_s}{\partial x} - mv\frac{\partial \ln p_s}{\partial y}. \tag{104}$$

When (103) is integrated vertically, it gives

$$\frac{\partial \ln p_s}{\partial t} = -\bar{D}^1 + \bar{N}^1_{p_s}, \tag{105}$$

using the following vertical integral notation

$$\overline{(\,)}^{\sigma} = \int_0^{\sigma} (\,)\, d\sigma. \tag{106}$$

Substituting (105) into (103) and integrating vertically from 0 to σ, yields

$$\dot{\sigma} = \sigma\overline{D}^1 - \overline{D}^{\sigma} - \left(\sigma\bar{N}^1_{p_s} - \bar{N}^{\sigma}_{p_s}\right). \tag{107}$$

The pressure vertical velocity, ω, is defined by

$$\frac{\omega}{p_s} = \frac{1}{p_s}\frac{dp}{dt} = \dot{\sigma} + \sigma\frac{d_H \ln p_s}{dt}. \tag{108}$$

Noting that

$$\frac{d_H \ln p_s}{dt} = -\overline{D}^1 + \bar{N}^1_{p_s} - N_{p_s}, \tag{109}$$

it follows that

$$\frac{\omega}{p_s} = -\overline{D}^{\sigma} + \bar{N}^{\sigma}_{p_s} - \sigma N_{p_s}. \tag{110}$$

N_{p_s} is only required for diagnostic calculation of $\dot{\sigma}$ and ω for the first time step, for which it is calculated using simple centred finite differencing. In C-CAM, a semi-Lagrangian evaluation of N_{p_s} is used for later time steps, as described in subsection 7.2.

6.2 Hydrostatic equation

The hydrostatic equation (102) may be integrated assuming a simple average layer virtual temperature between levels, to give

$$\phi_{v_k} = \phi_{v_{k-1}} - \frac{R_d}{2}\left(T_{v_k} + T_{v_{k-1}}\right) \ln \frac{\sigma_k}{\sigma_{k-1}} \quad \text{for } k = 2, 3, .., K. \tag{111}$$

For the lowest level, a standard temperature lapse from the surface of 6.5° km^{-1} gives

$$\phi_{v_1} = \phi_s - \left\{\sigma_1^{-0.0065 R_d/g} - 1\right\} \frac{R_d T_{v_1}}{0.0065}, \tag{112}$$

where g is the gravity constant. Thus the geopotential may be expressed linearly in terms of temperature in the form

$$\phi_{v_k} = \phi_{v_{k-1}} + \beta_k^- T_{v_{k-1}} + \beta_k T_{v_k} \quad \text{for } k = 1, 2, .., K \tag{113}$$

where ϕ_{v_0} is understood to equal ϕ_s the surface geopotential, i.e. gz_s, where $z_s$is the surface elevation. The final expression for the geopotential is thus of the form

$$\phi_{v_k} = \phi_s + \sum_{j=1}^{K} B_{kj} T_{v_j} \quad \text{for } k = 1, 2, .., K. \tag{114}$$

7 Semi-Lagrangian discretization

The primitive equations are now solved by two-time-level semi-Lagrangian discretization. Values at the current time level are denoted with superscript τ, those at the subsequent time level by $\tau + 1$, and those at the departure points at time τ (having arrival positions at the $\tau + 1$ grid points) by τ_*. The departure points are efficiently calculated as described in Section 3. Bicubic spatial interpolation is then used to evaluate all quantities with superscript τ_*, as also described in Section 3.

To avoid mountain resonances, Rivest et al. (1994) advocated off-centring of the time-averaged terms. This is included in the mass and thermodynamic equations below in terms of ε_a, a small constant having a typical value of 0.1; similar off-centring is included in the momentum equations in terms of ε_b, presently set to be identical to ε_a. The various equations will be discussed separately in the following subsections.

7.1 Semi-Lagrangian surface pressure equation

Evaluating the above primitive equations at the mid-points of the fluid trajectories, (100) becomes

$$\left\{\ln p_s + (1 + \varepsilon_a)\frac{\Delta t}{2}\left(D + \frac{\partial \dot{\sigma}}{\partial \sigma}\right)\right\}^{\tau+1}$$

$$= \left\{ \ln p_s - (1-\varepsilon_a)\frac{\Delta t}{2}\left(D + \frac{\partial \dot{\sigma}}{\partial \sigma}\right)\right\}^{\tau_*} = \frac{\Delta t}{2} M_{p_s} \text{ say.} \qquad (115)$$

Note that a special treatment for advection of surface pressure is usually used, as described in Section 8, to provide greater accuracy near steep terrain.

7.2 Semi-Lagrangian derivation of $\dot{\sigma}$ and ω/p_s

It is important to note that once the right-hand-side departure values of the continuity equation have been determined, the $\tau+1$ values of $\dot{\sigma}$ and ω/p_s may be derived. Integrating (115) vertically throughout the depth of the atmosphere provides

$$\left\{ \ln p_s + (1+\varepsilon_a)\frac{\Delta t}{2}\overline{D}^1 \right\}^{\tau+1} = \frac{\Delta t}{2}\overline{M_{p_s}}^1 = X_{p_s}, \text{ say.} \qquad (116)$$

Similarly to the derivation of (100), further integration of (107) yields

$$\dot{\sigma}^{\tau+1} = \left(\sigma \overline{D}^1 - \overline{D}^\sigma\right)^{\tau+1} + \left(\sigma \overline{M_{p_s}}^1 - \overline{M_{p_s}}^\sigma\right)/(1+\varepsilon_a). \qquad (117)$$

Substituting (100) into (108) also yields

$$\left(\frac{\omega}{p_s}\right)^{\tau+1} = -\left(\overline{D}^\sigma\right)^{\tau+1} + \left(\overline{M_{p_s}}^\sigma - \sigma M_{p_s}\right)/(1+\varepsilon), \qquad (118)$$

where now D, $\dot{\sigma}$ and ω/p_s are all consistently valid at $\tau+1$. Noticeably inferior performance was produced in an early version of the model, when M_{p_s} was approximated by N_{p_s} of (103) .

7.3 Semi-Lagrangian temperature equation

Equation (98) is first rearranged in terms of a reference temperature $\bar{T}$ to give

$$\frac{d_H T}{dt} - \frac{R_d \bar{T}}{c_p \sigma}\frac{\omega}{p_s} = N_T \qquad (119)$$

where

$$N_T = \tilde{N}_T + \frac{R_d(T-\bar{T})}{c_p \sigma}\frac{\omega}{p_s}. \qquad (120)$$

In C-CAM, $\bar{T}$ is prescribed each time step; it is allowed to vary horizontally, but not vertically. The vertical advection term has been omitted from (119), as it is calculated separately (as described in Section 5) by a split procedure at the beginning and end of the semi-Lagrangian "dynamics" calculations. Semi-Lagrangian discretization of (119) then gives

$$\left\{T-(1+\varepsilon_a)\frac{\Delta t}{2}\frac{R_d\bar{T}}{c_p\sigma}\frac{\omega}{p_s}\right\}^{\tau+1}=\left\{T+(1-\varepsilon_a)\frac{\Delta t}{2}\frac{R_d\bar{T}}{c_p\sigma}\frac{\omega}{p_s}\right\}^{\tau_*}+\Delta t N_T^{\bar{\tau}}$$

$$=A_T \text{ say.} \tag{121}$$

Here the superscript $\bar{\tau}$ represents an average along a trajectory between the τ_* and $\tau+1$ values of the bracketed quantities. The $\tau+1$ component of these terms is a little problematic; a time extrapolated value could be used, but usually in C-CAM it is assumed that these terms change slowly in time and can be adequately approximated by τ values at the appropriate spatial locations. Durran and Reinecke (2004) have suggested that these terms be treated by an Adams-Bashforth procedure; this has been implemented as an option in C-CAM, but no benefit has been observed from its use.

Equations (117) and (118) provide a separation of ω/p_s into further "linear" and "nonlinear" components (with respect to divergence, D). Substituting (118) into (121) gives the final semi-Lagrangian version of the temperature equation,

$$\left\{T+(1+\varepsilon_a)\frac{\Delta t}{2}\frac{R_d\bar{T}}{c_p\sigma}\overline{D}^{\sigma}\right\}^{\tau+1}=A_T+\frac{\Delta t}{2}\frac{R_d\bar{T}}{c_p\sigma}\left(\overline{M_{p_s}}^{\sigma}-\sigma M_{p_s}\right)=X_T \text{ say.} \tag{122}$$

Note that a special treatment for advection of the temperature variable in (121) is usually used, as described in Section 8, to provide greater accuracy near steep terrain.

7.4 Semi-Lagrangian momentum equations

Define an augmented geopotential

$$P_v=\phi_v+R_dT_v\ln p_s \tag{123}$$

and also a linearized augmented geopotential

$$P=\phi+R_d\bar{T}\ln p_s, \tag{124}$$

where ϕ is calculated using temperature rather than virtual temperature, and where the surface pressure term is multiplied by the reference temperature $\bar{T}$ (as defined in the previous section) rather than T_v. Equations (94) and (95) may be rearranged as

$$\frac{d_Hu}{dt}+m\frac{\partial P_v}{\partial x}=(f+f_m)v+\tilde{N}_u+mR_d\ln p_s\frac{\partial T_v}{\partial x}, \tag{125}$$

$$\frac{d_Hv}{dt}+m\frac{\partial P_v}{\partial y}=-(f+f_m)u+\tilde{N}_v+mR_d\ln p_s\frac{\partial T_v}{\partial y}. \tag{126}$$

For the semi-implicit solution, it is advantageous to write the left-hand-side in terms of P rather than P_v, whence

$$\frac{d_H u}{dt} + m\frac{\partial P}{\partial x} = (f + f_m)v + \tilde{N}_u + mR_d \ln p_s \frac{\partial T_v}{\partial x} + m\frac{\partial (P - P_v)}{\partial x}, \qquad (127)$$

$$\frac{d_H v}{dt} + m\frac{\partial P}{\partial y} = -(f + f_m)u + \tilde{N}_v + mR_d \ln p_s \frac{\partial T_v}{\partial y} + m\frac{\partial (P - P_v)}{\partial y}, \qquad (128)$$

where, as for temperature, the vertical advection terms are omitted because they are determined in a separate split calculation. Semi-Lagrangian discretization then produces

$$\left\{u + (1+\varepsilon_b)\frac{\Delta t}{2}\left(m\frac{\partial P}{\partial x} - fv\right)\right\}^{\tau+1} = \left\{u - (1-\varepsilon_b)\frac{\Delta t}{2}\left(m\frac{\partial P}{\partial x} - fv\right)\right\}^{\tau_*}$$

$$+\Delta t N_u^{\bar{\tau}} \qquad = A_u \text{ say}, \qquad (129)$$

$$\left\{v + (1+\varepsilon_b)\frac{\Delta t}{2}\left(m\frac{\partial P}{\partial y} + fu\right)\right\}^{\tau+1} = \left\{v - (1-\varepsilon_b)\frac{\Delta t}{2}\left(m\frac{\partial P}{\partial y} + fu\right)\right\}^{\tau_*}$$

$$+\Delta t N_v^{\bar{\tau}} \qquad = A_v \text{ say}, \qquad (130)$$

where now

$$N_u = \tilde{N}_u + f_m v + mR_d \ln p_s \frac{\partial T_v}{\partial x} + m\frac{\partial (P - P_v)}{\partial x}, \qquad (131)$$

$$N_v = \tilde{N}_v - f_m u + mR_d \ln p_s \frac{\partial T_v}{\partial y} + m\frac{\partial (P - P_v)}{\partial y}. \qquad (132)$$

7.4.1 Treatment of pressure gradient terms

There are important subtleties in the finite-differencing treatment of the above pressure gradient terms, as a result of the availability of reversible staggering. Note first that the eventual semi-implicit solver will be using staggered values of $u^{\tau+1}$ and $v^{\tau+1}$. To provide eventual consistency between the pressure gradient terms (in particular for any situation in which there has been no change at a grid point due to advection), all terms involving horizontal derivatives on the right-hand-sides of (129) to (132) are first evaluated at the staggered locations, then transformed reversibly to unstaggered positions for use in the right-hand-sides of (129) to (132). This procedure is necessary to gain the excellent dispersion characteristics outlined by McGregor (2005). It is a key ingredient in the excellent performance achieved by C-CAM. It is a technique that is not readily available to spectral models, or models formulated on other grids.

7.4.2 Re-organization of the momentum equations

Solving the simultaneous equations (129) and (130) in terms of $u^{\tau+1}$ and $v^{\tau+1}$ yields

$$\left\{u(1+F^2)+(1+\varepsilon_b)\frac{\Delta t}{2}m\left(\frac{\partial P}{\partial x}+F\frac{\partial P}{\partial y}\right)\right\}^{\tau+1}$$

$$= A_u + FA_v \quad = X_u \text{ say,} \tag{133}$$

$$\left\{v(1+F^2)+(1+\varepsilon_b)\frac{\Delta t}{2}m\left(\frac{\partial P}{\partial y}-F\frac{\partial P}{\partial x}\right)\right\}^{\tau+1}$$

$$= A_v - FA_u \quad = X_v \text{ say,} \tag{134}$$

where

$$F = (1+\varepsilon_b)f\Delta t/2. \tag{135}$$

Note that the reversible staggering procedure has avoided the averaging truncation errors of the Coriolis terms normally associated with a C-grid. Division of each of (133) and (134) by $m(1+F^2)$ gives

$$\left\{\frac{u}{m}+\frac{\Delta t}{2}\alpha\left(\frac{\partial P}{\partial x}+F\frac{\partial P}{\partial y}\right)\right\}^{\tau+1} = \frac{\alpha X_u}{m(1+\varepsilon_b)}, \tag{136}$$

$$\left\{\frac{v}{m}+\frac{\Delta t}{2}\alpha\left(\frac{\partial P}{\partial y}-F\frac{\partial P}{\partial x}\right)\right\}^{\tau+1} = \frac{\alpha X_v}{m(1+\varepsilon_b)}, \tag{137}$$

where

$$\alpha = (1+\varepsilon_b)/(1+F^2). \tag{138}$$

It is possible to further reorganize these equations to ensure that the final Helmholtz equation can consistently use a 5-point stencil. This is achieved by rewriting (136) and (137) as

$$\left\{\frac{u}{m}+\frac{\Delta t}{2}\left(\frac{\partial \alpha P}{\partial x}+\frac{\partial \alpha FP}{\partial y}-\alpha_3 P\right)\right\}^{\tau+1} = \frac{\alpha X_u}{m(1+\varepsilon_b)}, \tag{139}$$

$$\left\{\frac{v}{m}+\frac{\Delta t}{2}\left(\frac{\partial \alpha P}{\partial y}-\frac{\partial \alpha FP}{\partial x}-\alpha_4 P\right)\right\}^{\tau+1} = \frac{\alpha X_v}{m(1+\varepsilon_b)}, \tag{140}$$

where

$$\alpha_3 = \frac{\partial \alpha}{\partial x}+\frac{\partial \alpha F}{\partial y}, \tag{141}$$

$$\alpha_4 = \frac{\partial \alpha}{\partial y}-\frac{\partial \alpha F}{\partial x}. \tag{142}$$

are evaluated by first-order finite differencing at the staggered u and v positions respectively.

7.5 The semi-implicit solution procedure

Substituting (114), using T rather than T_v, into the definition (124) for the linearized augmented height $P^{\tau+1}$ gives

$$P_k^{\tau+1} = \phi_s + \sum_{j=1}^{K} B_{kj} T_j^{\tau+1} + R_d \bar{T} \ln p_s^{\tau+1}. \tag{143}$$

Then substituting for $T^{\tau+1}$ and $p_s^{\tau+1}$ from (122) and (116) yields

$$\begin{aligned} P_k^{\tau+1} &= \phi_s - (1+\varepsilon_a)\frac{\Delta t}{2}\frac{R_d \bar{T}}{c_p}\sum_{j=1}^{K}\frac{B_{kj}}{\sigma_j}\overline{D^{\tau+1}}^{\sigma_j} + \sum_{j=1}^{K} B_{kj}(X_T)_j \\ &\quad + R_d \bar{T}\left(X_{p_s} - (1+\varepsilon_a)\frac{\Delta t}{2}\overline{D^{\tau+1}}^{1}\right). \end{aligned} \tag{144}$$

Collecting the divergence terms, the equation may be rewritten in terms of $D^{\tau+1}$,

$$P_k^{\tau+1} + (1+\varepsilon_a)\frac{\Delta t}{2}\sum_{j=1}^{K} C_{kj} D_j^{\tau+1} = X_P \tag{145}$$

where

$$X_P = \phi_s + \sum_{j=1}^{K} B_{kj}(X_T)_j + R_d \bar{T} X_{p_s}. \tag{146}$$

The matrix $\mathbf{C}$ has constant coefficients which are a function of the reference temperature, the choice of σ levels, and the choice of discretization for vertical integration. For simple trapezoidal vertical integration,

$$C_{kj} = R_d \bar{T}(\sigma_{j-1/2} - \sigma_{j+1/2}) + \frac{R_d \bar{T}}{c_p}\sum_{n=j}^{K} B_{kj}\frac{\Delta^+ \sigma_j}{\sigma_n}, \tag{147}$$

where

$$\Delta^+ \sigma_K = \sigma_K; \;\; \Delta^+ \sigma_j = \sigma_j - \sigma_{j+1} \text{ for } 1 \le j < K. \tag{148}$$

The system of equations (139), (140) and (145) may be decoupled in the vertical by determining the eigenvalues λ of $\mathbf{C}$ and the corresponding eigenvector matrix $\mathbf{E}$, to satisfy

$$\sum_{j=1}^{K} C_{kj} E_{jn} = E_{kn}\lambda_n. \tag{149}$$

Now $u^{\tau+1}$, $v^{\tau+1}$, $D^{\tau+1}$, $P^{\tau+1}$, X_u, X_v and X_P are expanded in terms of their vertical modes $\mathcal{U}$, $\mathcal{V}$, $\mathcal{D}$, $\mathcal{P}$, $\mathcal{X}_u$, $\mathcal{X}_v$and $\mathcal{X}_P$; for example

$$u_k^{\tau+1} = \sum_{j=1}^{K} E_{kj}\mathcal{U}_j. \tag{150}$$

It was noted earlier that $\bar{T}$ is allowed to vary horizontally in C-CAM, the only requirement being that it does not change during a time step. To simplify the calculation of eigenvectors, they are pre-calculated with respect to a reference temperature of 300 K, from the equation

$$\sum_{j=1}^{K} \left(\frac{300}{\bar{T}} C_{kj} \right) E_{jn} = E_{kn}\lambda_{n300}. \tag{151}$$

It is clear from the above that the eigenvectors of (149) and (151) are identical, and that the eigenvalues are related to the pre-calculated values by

$$\lambda_n = \frac{\bar{T}}{300}\lambda_{n300} \text{ for} n = 1 \text{to} K. \tag{152}$$

It may also be noted that this more general definition of $\bar{T}$ succeeds because the subsequent equations do not involve any horizontal derivatives of λ (and thus $\bar{T}$).

The equations in eigenvector space corresponding to (139), (140) and (145) become

$$\frac{\mathcal{U}}{m} + \frac{\Delta t}{2}\left(\frac{\partial \alpha \mathcal{P}}{\partial x} + \frac{\partial \alpha F \mathcal{P}}{\partial y} - \alpha_3 \mathcal{P} \right) = \frac{\alpha \mathcal{X}_u}{m(1+\varepsilon_b)}, \tag{153}$$

$$\frac{\mathcal{V}}{m} + \frac{\Delta t}{2}\left(\frac{\partial \alpha \mathcal{P}}{\partial y} - \frac{\partial \alpha F \mathcal{P}}{\partial x} - \alpha_4 \mathcal{P} \right) = \frac{\alpha \mathcal{X}_v}{m(1+\varepsilon_b)}, \tag{154}$$

$$\mathcal{P}_k + (1+\varepsilon_a)\frac{\Delta t}{2}\lambda_k \mathcal{D}_j = \mathcal{X}_P. \tag{155}$$

The divergence is given by (101), so (153) and (154) can be combined by horizontal differentiation to yield the divergence in the form

$$\mathcal{D} = -m^2 \frac{\Delta t}{2}\nabla_\alpha^2 \mathcal{P} + \mathcal{X}_D \tag{156}$$

where

$$\mathcal{X}_D = \frac{m^2}{(1+\varepsilon_b)}\left\{ \frac{\partial(\alpha \mathcal{X}_u/m)}{\partial x} + \frac{\partial(\alpha \mathcal{X}_v/m)}{\partial y} \right\} \tag{157}$$

and the 5-point Laplacian operator is defined by

$$(\Delta x)^2 \nabla_\alpha^2 \mathcal{P} \quad = \quad \alpha_{i+1,j}\mathcal{P}_{i+1,j} + \alpha_{i-1,j}\mathcal{P}_{i-1,j} + \alpha_{i,j+1}\mathcal{P}_{i,j+1} + \alpha_{i,j-1}\mathcal{P}_{i,j-1}$$

$$-4\alpha_{i,j}\mathcal{P}_{i,j} + \frac{\Delta x}{2}\left\{\alpha_{3_{i-.5,j}}(\mathcal{P}_{i-1,j} + \mathcal{P}_{i,j}) - \alpha_{3_{i+.5,j}}(\mathcal{P}_{i+1,j} + \mathcal{P}_{i,j})\right\}$$

$$+\frac{\Delta x}{2}\left\{\alpha_{4_{i,j-.5}}(\mathcal{P}_{i,j-1} + \mathcal{P}_{i,j}) - \alpha_{4_{i,j+.5}}(\mathcal{P}_{i,j+1} + \mathcal{P}_{i,j})\right\} \qquad (158)$$

where only the horizontal (i, j) indexing is shown, and use has been made of the equivalence of Δx and Δy. Note that the arrangement of terms in (153) and (154) avoids the appearance of cross-derivative terms in (158) involving $\alpha F\mathcal{P}$. A simple rearrangement of (158) gives

$$\begin{aligned}(\Delta x)^2\nabla_\alpha^2\mathcal{P} &= (\alpha_{i+1,j} - \alpha_{3_{i+.5,j}})\mathcal{P}_{i+1,j} + (\alpha_{i-1,j} + \alpha_{3_{i-.5,j}})\mathcal{P}_{i-1,j} \\ &+(\alpha_{i,j+1} - \alpha_{4_{i,j+.5}})\mathcal{P}_{i,j+1} + (\alpha_{i,j-1} + \alpha_{4_{i,j-.5}})\mathcal{P}_{i,j-1} \\ &+(\alpha_{3_{i-.5,j}} - \alpha_{3_{i+.5,j}} + \alpha_{4_{i,j-.5}} - \alpha_{4_{i,j+.5}} - 4\alpha_{i,j})\mathcal{P}_{i,j} \qquad (159)\end{aligned}$$

This equation is of the form

$$\begin{aligned}(\Delta x)^2\nabla_\alpha^2\mathcal{P} = \alpha'_{i+1,j}\mathcal{P}_{i+1,j} + \alpha'_{i-1,j}\mathcal{P}_{i-1,j} + \alpha'_{i,j+1}\mathcal{P}_{i,j+1} + \alpha'_{i,j-1}\mathcal{P}_{i,j-1} \\ -4\alpha'_{i,j}\mathcal{P}_{i,j} \qquad (160)\end{aligned}$$

where each α' is approximately equal to 1. Substituting (156) into (155) yields the Helmholtz equation for $\mathcal{P}$

$$\mathcal{P} - m^2\frac{\Delta t^2}{4}(1+\varepsilon_a)\lambda_k\nabla_\alpha^2\mathcal{P} = \mathcal{X}_P - \frac{\Delta t}{2}(1+\varepsilon_a)\lambda_k\mathcal{X}_D. \qquad (161)$$

7.6 Solution of the Helmholtz equation

The Helmholtz equation (161) is an equation of the form

$$A\mathcal{P} - \Delta x^2\nabla_\alpha^2\mathcal{P} = B. \qquad (162)$$

This Helmholtz equation (162) is solved by successive over-relaxation (SOR) for each of the levels in vertical eigenvector space, giving an updated value each iteration as

$$\begin{aligned}\mathcal{P}'_{i,j} &= \mathcal{P}_{i,j} + \varpi\left\{\frac{\alpha'_{i+1,j}\mathcal{P}_{i+1,j} + \alpha'_{i-1,j}\mathcal{P}_{i-1,j}}{A_{i,j} + 4\alpha'_{i,j}}\right\} \\ &+\varpi\left\{\frac{\alpha'_{i,j+1}\mathcal{P}_{i,j+1} + \alpha'_{i,j-1}\mathcal{P}_{i,j-1} + B_{i,j}}{A_{i,j} + 4\alpha'_{i,j}} - \mathcal{P}_{i,j}\right\} \qquad (163)\end{aligned}$$

where ϖ denotes an acceleration factor, which is expected to lie between 1 and 2. The values of ϖ depend on the number of grid points N, the Schmidt magnification factor S, and the eigenvalues. It was not possible to derive an analytic expression for the optimum acceleration factor. Optimum values were determined experimentally for a wide range of values and interpolation used between these values (courtesy of Martin Dix). An alternative conjugate-gradient solution is also available, implemented and tested by Martin Dix.

It was shown by Young (1971) that two-dimensional Poisson or Helmholtz equations may be solved with SOR using a red-black (or checkerboard) configuration arrangement, with the same convergence rates as for the standard SOR scheme. For the conformal-cubic geometry, this translates to a three-colour arrangement, as illustrated in Fig. 9. The big advantage of checkerboard schemes is that they permit easy vectorization. The procedure is that (163) is used during each iteration to first update all the red points, then all the green points, then all the blue points. Note that during a single-colour update, none of the other-coloured points are being altered, and so each single-colour update can be done as a single vector sweep.

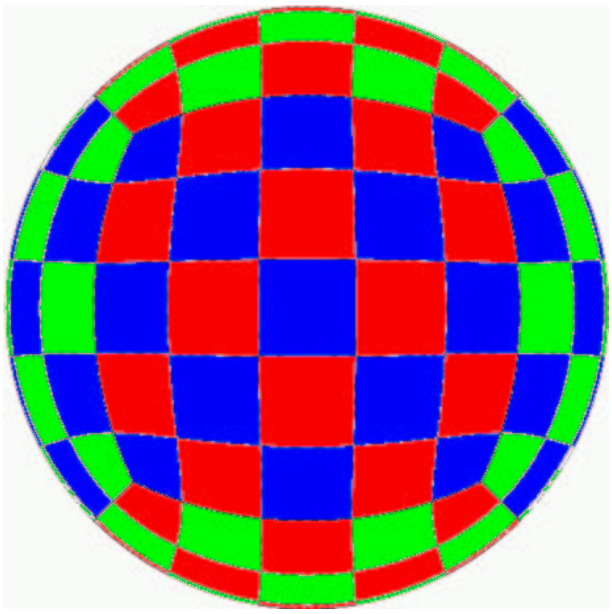

Figure 9: Diagram showing the 3-colour scheme used for the solution of the Helmholtz equation, illustrated on a C5 grid.

7.7 Inversion to physical space

Having obtained values for $\mathcal{P}$, the eigenvectors may be used to give $P^{\tau+1}$ from (150). The velocity equations (139) and (140) then give $u^{\tau+1}$ and $v^{\tau+1}$ at their staggered locations. Calculation of the corresponding divergences from (101) then provides $p_s^{\tau+1}$ from (116) and $T^{\tau+1}$ from (122). Finally, $u^{\tau+1}$ and $v^{\tau+1}$ are transformed to their unstaggered locations.

8 Horizontal advection near orography

The innovations of this section significantly avoid problems of advective overshooting of surface pressure and temperature near steep terrain. These innovations avoid any necessity to introduce "hybrid" vertical coordinates.

8.1 Horizontal advection of surface pressure

In (115) it is required to find a departure-point value of a function similar to $\ln p_s$, for advection along a σ-surface. For simplicity, the present discussion is given in terms of $\ln p_s$, although in practice the combined right-hand-side variable is used. To reduce truncation errors near steep orography, an associated variable $\ln \breve{p}_s$ is also advected. We define

$$\ln \breve{p}_s = \ln p_s + \frac{z_s g}{R_d \overline{T}_k}, \tag{164}$$

where $\overline{T}_k$ is some reference temperature, presently set to 300 K. The transformed variable has much less orographic variation than $\ln p_s$, as use has been made of an approximate reduction to mean sea-level pressure via the hydrostatic equation (102). Formally,

$$(\ln p_s)^* = (\ln \breve{p}_s)^* - \left(\frac{z_s g}{R_d \overline{T}_k}\right)^*. \tag{165}$$

The right-hand-side terms are evaluated, respectively, by cubic interpolation and bi-linear interpolation. The assumption is made everywhere within C-CAM, without loss of generality, that the orography data set exactly satisfies a bi-linear relationship. The upstream orographic determination can thus be considered "exact", which leads to enhanced accuracy from the usage of (165).

8.2 Horizontal advection of temperature

In (121) it is required to find a departure-point value for the right-hand-side function derived from T, for advection along a σ-surface. As for surface pressure, a simpler discussion is given here for T, omitting the extra terms for this discussion. To reduce truncation errors near steep orography, an associated variable $\breve{T}$ is set up. We define

$$\breve{T}_k = T_k + 0.0065 \gamma_k z_s, \tag{166}$$

where

$$\gamma_k = 0 \ \text{ for } \sigma_k \leq 0.2, \tag{167}$$

$$\gamma_k = 5\sigma_k - 1 \ \text{ for } 0.2 \leq \sigma_k \leq 0.4, \tag{168}$$

$$\gamma_k = 1 \ \text{ for } 0.4 \leq \sigma_k. \tag{169}$$

This transformed temperature variable has rather less orographic variation than T, having made use of a standard lapse rate, and thus leads to smaller interpolation errors during advective calculations. Simulation results seem to be not particularly sensitive to the precise form of γ_k. As for surface pressure, formally

$$(T_k)^* = \left(\breve{T}_k\right)^* - (0.0065\gamma_k z_s)^* \tag{170}$$

and, again, the right-hand-side terms are evaluated, respectively, by cubic interpolation and bi-linear interpolation.

9 Mass and moisture conservation

During each time step it is required that the global averages of mass and moisture do not change as a result of advective and other "dynamics" processes.

Mass conservation

First, the method will be described for mass conservation. The following measure of the globally integrated mass before the "dynamics" is calculated,

$$\overline{M}^a = \sum_{ij=1}^{6N^2} \frac{p^a_{s_{ij}}}{m^2_{ij}}, \tag{171}$$

where one-dimensional indexing of the form ij has been adopted. The uncorrected value of $p_{s_{ij}}$ after the "dynamics" is denoted by $p^b_{s_{ij}}$ and its increment is written as

$$\Delta p_{s_{ij}} = p^b_{s_{ij}} - p^a_{s_{ij}}. \tag{172}$$

Now denote the globally-integrated positive increment by

$$\Delta M^+ = \sum_{ij=1}^{6N^2} \frac{\max(0, \Delta p_{s_{ij}})}{m^2_{ij}} \tag{173}$$

and the integrated negative increment by

$$\Delta M^- = \sum_{ij=1}^{6N^2} \frac{\min(0, \Delta p_{s_{ij}})}{m^2_{ij}}. \tag{174}$$

A factor α_p is next defined as

$$\alpha_p = \sqrt{-\frac{\Delta M^-}{\Delta M^+}}. \tag{175}$$

The expression used for the final corrected value, $p^c_{s_{ij}}$, is

$$p^c_{s_{ij}} = p^a_{s_{ij}} + \alpha_p \max(0, \Delta p_{s_{ij}}) + \frac{1}{\alpha_p} \min\left(0, \Delta p_{s_{ij}}\right). \tag{176}$$

It can then be verified by substitution that the integrated value of (176) satisfies

$$\sum_{ij=1}^{6N^2} \frac{p^c_{s_{ij}}}{m^2_{ij}} = \sum_{ij=1}^{6N^2} \frac{p^a_{s_{ij}}}{m^2_{ij}}. \tag{177}$$

The motivation for (176) is that the correction for values of surface pressure should be directly proportional to its "dynamics" increment ΔM_{ij}, but the sign of the correction should depend on the sign of the increment.

Moisture conservation

A related, but slightly more complicated, method will now be given for conserving the integrated water vapour mixing ratio, q. The same technique applies for the other water components and for other trace gases. The following measure of the globally integrated water vapour before the "dynamics" is used,

$$\overline{Q}^a = \sum_{k=1}^{K} \sum_{ij=1}^{6N^2} p^a_{s_{ij}} q^a_{ij,k} \frac{|\Delta\sigma_k|}{m^2_{ij}}. \tag{178}$$

The uncorrected value of q after the "dynamics" is denoted by $q^b_{ij,k}$ and an effective mass-weighted increment is written as

$$\Delta Q_{ij,k} = p^c_{s_{ij}} \max(q^b_{ij,k}, q_{min}) - p^a_{s_{ij}} q^a_{ij,k}, \tag{179}$$

where q_{min} denotes the minimum physically permitted value of q, typically chosen as 10^{-6}, a little less than the lowest value observed by McCormick et al. (1993). Next, denote the integrated positive increment by

$$\Delta Q^+ = \sum_{k=1}^{K} \sum_{ij=1}^{6N^2} \max(0, \Delta Q_{ij,k}) \frac{|\Delta\sigma_k|}{m^2_{ij}} \tag{180}$$

and the integrated negative increment by

$$\Delta Q = \sum_{k=1}^{K} \sum_{ij=1}^{6N^2} \min(0, \Delta Q_{ij,k}) \frac{|\Delta\sigma_k|}{m^2_{ij}}. \tag{181}$$

A factor α_q is next defined as

$$\alpha_q = \min\left(-\frac{\Delta Q^-}{\Delta Q^+}, \sqrt{-\frac{\Delta Q^-}{\Delta Q^+}}\right). \tag{182}$$

The expression used for the final corrected value, $q^c_{ij,k}$, is

$$p^c_{s_{ij}}\, q^c_{ij,k} = p^a_{s_{ij}}\, q^a_{ij,k} + \alpha_q \max(0, \Delta Q_{ij,k}) + \frac{\min(0, \Delta Q_{ij,k})}{\max(1, \alpha_q)}. \tag{183}$$

It can then be verified by substitution that the integrated value of (183) is equal to the left-hand-side of (178), i. e.,

$$\sum_{k=1}^{K} \sum_{ij=1}^{6N^2} p^c_{s_{ij}}\, q^c_{ij,k} \frac{|\Delta\sigma_k|}{m^2_{ij}} = \sum_{k=1}^{K} \sum_{ij=1}^{6N^2} p^a_{s_{ij}}\, q^a_{ij,k} \frac{|\Delta\sigma_k|}{m^2_{ij}}. \tag{184}$$

The formula also produces $q^c_{ij,k} \geq q_{min}$ at each grid point. As for mass correction, the motivation for (183) is that the correction for each moisture concentration should be directly proportional to its "dynamics" increment $\Delta Q_{ij,k}$, but the sign of the correction should depend on the sign of the increment.

10 Some time stepping considerations

10.1 The first two time steps

Being a two-time-level model, extra care is taken at the beginning of each simulation to provide suitably accurate advective velocities. For the first two time steps, (64) can not be used to provide velocities at the half-time levels. The following procedure is used to get around this difficulty.

First (trial) half time step ($\tau = 1/2$)

The dynamics (only) is integrated for half a time step, using as a trial advective velocity $\mathbf{u}^0$. This produces a prognostic value for $\mathbf{u}^{1/2}$.

First time step ($\tau = 1$)

The model integration starts afresh, using $\mathbf{u}^{1/2}$as the advective velocity.

Second time step ($\tau = 2$)

The integration continues, using $(3\mathbf{u}^1 - \mathbf{u}^0)/2$ as $\mathbf{u}^{1+1/2}$, the advective velocity.

10.2 Procedure for calling dynamics and physics

C-CAM has been organized so that the "dynamics" and "physics" are performed sequentially in "split" mode, as first advocated by Marchuk (1974). Whilst this provides numerical stability, and assists code modularity, it can lead to some time truncation errors when using large time steps. The following procedure has been adopted in C-CAM, and found to be both robust and beneficial. The description is given just in terms of u, but all model variables are similarly involved. The intermediate model values after "dynamics" and "physics" are denoted respectively by u_d and u_p. The nonlinear term $\tilde{N}_u$ refers to the term appearing in (94).

First time step

Set $\tilde{N}_u^1$=0.
Dynamics and physics produce u_d^1 and u_p^1.
Define $\tilde{N}_u^2 = (u_p^1 - u_d^1)/\Delta t$.
Set $u^1 = u_d^1$.

Later time step τ

Use $\tilde{N}_u^\tau$ from preceding time step.
Dynamics and physics produce u_d^τ and u_p^τ.
Define $\tilde{N}_u^{\tau+1} = (u_p^\tau - u_d^\tau)/\Delta t$.
Set $u^\tau = u_d^\tau$.

Writing model output

Whenever model output is written at the end of a time step, the u_p^τ values are written so as to incorporate the full updating effect of the physics.

11 Nudging options for stretched simulations

For some C-CAM applications, a nudging tendency may be applied at the end of a time step to selected variables. For example, for the u component, the nudging tendency equation, in split form, is

$$\frac{\partial u}{\partial t} = \frac{u_{LS} - u}{\tau_{\text{efold}}}. \tag{185}$$

If the value of u before the nudging correction is denoted by u', the analytic solution of (185) is

$$u^{\tau+1} = u_{LS} + \exp\left(\frac{\Delta t}{\tau_{\text{efold}}}\right)(u' - u_{LS}). \tag{186}$$

From (186), it can be seen that if the nudging is applied for a time interval equal to τ_{efold}, then the difference of u from u_{LS} will be reduced during that time interval by a factor exp(1). In practice, the following simple finite difference solution to (185) is used

$$u^{\tau+1} = u' + \Delta t(u_{LS} - u'). \tag{187}$$

Currently, with C-CAM, options exist for nudging the wind components above about 800 m. For some applications, it is desired to minimize chaotic climate effects such that the large-scale systems approximately follow a specified set of synoptic systems, say from reanalyses or from a coupled GCM. For such applications, the winds are weakly nudged at every grid point with an e-folding time of around 48 h.

A number of long climate downscaling runs have been performed with moderate stretching of S = 3.33. For these runs, far-field wind nudging has been used to assure reasonable climatology in the coarsest parts of the domain. For such applications, there is no nudging on the central panel, or on the inner half of each of the adjacent four panels. On the furthest panel τ_{efold}= 24 h is

usually used, with its inverse value linearly decreasing to zero at the half-panel boundaries. An example of the nudging weights is shown in Fig. 10.

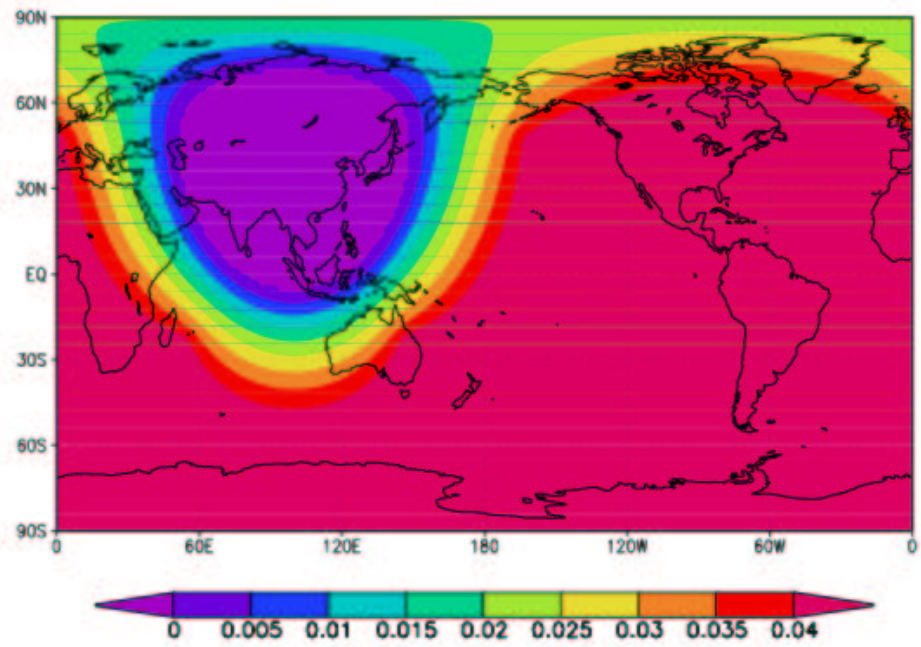

Figure 10: An example of nudging weights, the inverse of τ_{efold} (h^{-1}), as used in 60 km resolution simulations centred over Asia with a C63 grid.

Acknowledgments. The author is grateful to Jim Purser for generously providing his algorithm for calculating the basic grid information of the conformal-cubic grid, and for suggesting use of the Vandermonde method in deriving the reversible staggering formulae. Martin Dix has provided a number of improvements to the C-CAM dynamics, especially regarding the Helmholtz solver; he has also assisted greatly by carefully checking this manuscript.

References

Arakawa, A., and V. R. Lamb, 1977: Computational design of the basic dynamical processes of the UCLA general circulation model. *Methods Comput. Phys.*, **17**, 173–265.

Durran, D., 1999: *Numerical methods for wave equations in GFD.* Springer Verlag, New York, 465 pp.

Durran, D. R., and P. A. Reinecke, 2004: Instability in explicit two-time-level semi-Lagrangian schemes. *Q. J. R. Meteorol. Soc.*, **130**, 365–369.

Gordon, H. B., L. D. Rotstayn, J. L. McGregor, M. R. Dix, E. A. Kowalczyk, S. P. O'Farrell, L. J. Waterman, A. C. Hirst, S. G. Wilson, M. A. Collier, I. G. Watterson, and T. I. Elliott, 2002: The CSIRO Mk3 climate system model. Technical Report 60, CSIRO Atmospheric Research, 130 pp.

Marchuk, G. I., 1974: *Numerical Methods in Weather Prediction.* Academic Press, New York, 277 pp.

McCormick, M. P., E. W. Chiou, L. R. McMaster, W. P. Chu, J. C. Larsen, D. Rind, and S. Oltmans, 1993: Annual variations of water vapor in the stratosphere and upper troposphere observed by the Stratospheric Aerosol and Gas Experiment II. *J. Geophys. Res.*, **98**, 4867–4874.

McGregor, J. L., 1993: Economical determination of departure points for semi-Lagrangian models. *Mon. Wea. Rev.*, **121**, 221–230.

McGregor, J. L., 1996: Semi-Lagrangian advection on conformal-cubic grids. *Mon. Wea. Rev.*, **124**, 1311–1322.

McGregor, J. L., 1997: Semi-Lagrangian advection on a cubic gnomonic projection of the sphere. *Numerical Methods in Atmospheric and Oceanic Modelling. The André J. Robert Memorial Volume*, C. Lin, R. Laprise, and H. Ritchie, Eds., (companion volume to Atmos.–Ocean), 153–169.

McGregor, J. L., 2005: Geostrophic adjustment for reversibly staggered grids. *Mon. Wea. Rev.*, **133**, 1119–1128.

McGregor, J. L., and M. R. Dix, 1997: Development of a global conformal-cubic primitive equations model. *Research Activities in Atmospheric and Oceanic Modelling Report No. 25, WMO/TD-No. 792*, A. Staniforth, Ed., 3.27–3.28.

McGregor, J. L., and M. R. Dix, 1998: A conformal-cubic atmospheric general circulation model. *Research Activities in Atmospheric and Oceanic Modelling Report No. 27, WMO/TD-No. 865*, A. Staniforth, Ed., 322–323.

McGregor, J. L., and M. R. Dix, 2001: The CSIRO conformal-cubic atmospheric GCM. *IUTAM Symposium on Advances in Mathematical Modelling of Atmosphere and Ocean Dynamics*, P. F. Hodnett, Ed., Kluwer, 197–202.

McGregor, J. L., and J. J. Katzfey, 1998: NWP experiments with a variable-resolution conformal-cubic primitive equations model. *Research Activities in Atmospheric and Oceanic Modelling Report No. 27, WMO/TD-No. 865*, A. Staniforth, Ed., 320–321.

McGregor, J. L., and J. J. Katzfey, 1999: Simulating typhoon recurvature with a variable-resolution conformal-cubic model. *Research Activities in Atmospheric and Oceanic Modelling Report No. 28, WMO/TD-No. 942*, H. Ritchie, Ed., 3.19–3.20.

McGregor, J. L., and L. M. Leslie, 1977: On the selection of grids for semi-implicit schemes. *Mon. Wea. Rev.*, **105**, 236–238.

McGregor, J. L., H. B. Gordon, I. G. Watterson, M. R. Dix, and L. D. Rotstayn, 1993: The CSIRO 9-level atmospheric general circulation model. Technical Report 26, CSIRO Atmospheric Research, 89 pp.

Nagata, M., L. M. Leslie, H. Kamahori, R. Nomura, H. Mino, Y. Kurihara, E. Rogers, R. L. Elsberry, B. K. Basu, A. Buzzi, J. Calvo, M. Desgagné, M. D'Isidoro, S.-Y. Hong, J. J. Katzfey, D. Majewski, P. Malguzzi, J. L. McGregor, A. Murata, J. Nachamkin, M. Roch, and C. Wilson, 2001: A mesoscale model intercomparison: a case of explosive development of a tropical cyclone (COMPARE III). *J. Meteor. Soc. Japan*, **79**, 999–1033.

Rancic, M., R. J. Purser, and F. Mesinger, 1996: A global shallow-water model using an expanded spherical cube: Gnomonic versus conformal coordinates. *Quart. J. Roy. Meteor. Soc.*, **122**, 959–982.

Randall, D. A., 1994: Geostrophic adjustment and the finite-difference shallow-water equations. *Mon. Wea. Rev.*, **122**, 1371–1377.

Ritchie, H., C. Temperton, A. Simmons, M. Hortal, T. Davies, D. Dent, and M. Hamrud, 1995: Implementation of the semi-Lagrangian method in a high-resolution version of the ECMWF forecast model. *Mon. Wea. Rev.*, **123**, 489–514.

Rivest, C., A. Staniforth, and A. Robert, 1994: Spurious resonant response of semi-Lagrangian discretizations to orographic forcing: Diagnosis and solution. *Mon. Wea. Rev.*, **122**, 366–376.

Roe, P. L., 1985: Some contributions to the modeling of discontinuous flows. *Lecture Notes in Applied Mathematics*, Springer-Verlag, New York, Volume 22, pp. 163–193.

Sadourny, R., 1972: Conservative finite-difference approximations of the primitive equations on quasi-uniform spherical grids. *Mon. Wea. Rev.*, **100**, 136–144.

Schmidt, F., 1977: Variable fine mesh in spectral global model. *Beitr. Phys. Atmos.*, **50**, 211–217.

Smagorinsky, J., S. Manabe, and J. L. Holloway, 1965: Numerical results from a nine-level general circulation model of the atmosphere. *Mon. Wea. Rev.*, **93**, 727–768.

Temperton, C., 1975: Algorithms for the solution of cyclic tridiagonal systems. *J. Comp. Phys.*, **19**, 317–323.

Temperton, C., and A. Staniforth, 1987: An efficient two-time-level semi-Lagrangian semi-implicit scheme. *Quart. J. Roy. Meteor. Soc.*, **113**, 1025–1039.

Thuburn, J., 1993: Use of a flux-limited scheme for vertical advection in a GCM. *Quart. J. Roy. Meteor. Soc.*, **119**, 469–487.

Van Leer, B., 1974: Towards the ultimate conservative difference scheme. II. Monotonicity and conservation combined in a second-order scheme. *J. Comput. Phys.*, **14**, 361–370.

Van Leer, B., 1977: Towards the ultimate conservative difference scheme IV. A new approach to numerical convection. *J. Comput. Phys.*, **23**, 276–299.

Winninghoff, F. J., 1968: On the adjustment toward a geostrophic balance in a simple primitive equation model with application to the problems of initialization and objective analysis. Ph.D. thesis, University of California, Los Angeles.

Young, D. M., 1971: *Iterative solution of large linear systems.* Academic Press, New York, 570 pp.